



**HAL**  
open science

# Multifractal desynchronization of the cardiac excitable cell network during atrial fibrillation. I. Multifractal analysis of clinical data

Guillaume Attuel, E. Gerasimova-Chechkina, Françoise Argoul, Hussein Yahia, A. Arneodo

## ► To cite this version:

Guillaume Attuel, E. Gerasimova-Chechkina, Françoise Argoul, Hussein Yahia, A. Arneodo. Multifractal desynchronization of the cardiac excitable cell network during atrial fibrillation. I. Multifractal analysis of clinical data. *Frontiers in Physiology*, 2017, pp.1-30. hal-01673364v2

**HAL Id: hal-01673364**

**<https://inria.hal.science/hal-01673364v2>**

Submitted on 26 Jan 2018 (v2), last revised 28 Mar 2018 (v4)

**HAL** is a multi-disciplinary open access archive for the deposit and dissemination of scientific research documents, whether they are published or not. The documents may come from teaching and research institutions in France or abroad, or from public or private research centers.

L'archive ouverte pluridisciplinaire **HAL**, est destinée au dépôt et à la diffusion de documents scientifiques de niveau recherche, publiés ou non, émanant des établissements d'enseignement et de recherche français ou étrangers, des laboratoires publics ou privés.

# Multifractal desynchronization of the cardiac excitable cell network during atrial fibrillation.

## I. Multifractal analysis of clinical data

G. Attuel<sup>1</sup>, E. Gerasimova-Chechkina<sup>2</sup>, F. Argoul<sup>3</sup>, H. Yahia<sup>1</sup> and  
A. Arneodo<sup>3,\*</sup>

<sup>1</sup>*Geometry and Statistics in acquisition data, Centre de Recherche INRIA, Bordeaux Sud-Ouest, 200 rue de la Vieille Tour, 33405 Talence Cedex, France*

<sup>2</sup>*Laboratory of Physical Foundation of Strength, Institute of Continuous Media Mechanics UB RAS, Perm, Russia*

<sup>3</sup>*Université de Bordeaux, CNRS, Laboratoire Ondes et Matière d'Aquitaine, UMR 5798, 33405 Talence, France*

Correspondence\*: Alain Arneodo, alain.arneodo@u-bordeaux.fr

## 2 ABSTRACT

3 Atrial fibrillation (AF) is a cardiac arrhythmia characterized by rapid and irregular atrial electrical  
4 activity with a high clinical impact on stroke incidence. Best available therapeutic strategies  
5 combine pharmacological and surgical means. But when successful, they do not always prevent  
6 long-term relapses. Initial success becomes all the more tricky to achieve as the arrhythmia  
7 maintains itself and the pathology evolves into sustained or chronic AF. This raises the open crucial  
8 issue of deciphering the mechanisms that govern the onset of AF as well as its perpetuation. In  
9 this study, we develop a wavelet-based multi-scale strategy to analyze the electrical activity of  
10 human hearts recorded by catheter electrodes, positioned in the coronary sinus (CS), during  
11 episodes of chronic AF. We compute the so-called multifractal spectra using two variants of  
12 the wavelet transform modulus maxima method, the moment (partition function) method and  
13 the magnitude cumulant method. Application of these methods to long time series recorded in  
14 a patient with chronic AF provides quantitative evidence of the multifractal intermittent nature  
15 of the electric energy of passing cardiac impulses at low frequencies, *i.e.* for times ( $\gtrsim 0.5$  s)  
16 longer than the mean interbeat ( $\simeq 10^{-1}$ s). We also report the results of a two-point magnitude  
17 correlation analysis which infers the absence of a multiplicative time-scale structure underlying  
18 multifractal scaling. The electric energy dynamics looks like a “multifractal white noise” with  
19 quadratic (log-normal) multifractal spectra. These observations challenge concepts of functional  
20 reentrant circuits in mechanistic theories of AF, still leaving open the role of the autonomic nervous  
21 system (ANS). A transition is indeed observed in the computed multifractal spectra which group  
22 according to two distinct areas, consistently with the anatomical substrate binding to the CS,  
23 namely the left atrial posterior wall, and the ligament of Marshall which is innervated by the  
24 ANS. In a companion paper (II. Modeling), we propose a mathematical model of a denervated  
25 heart where the kinetics of gap junction conductance alone induces a desynchronization of the  
26 myocardial excitable cells, accounting for the multifractal spectra found experimentally in the left  
27 atrial posterior wall area.

28 **Keywords:** Mechanisms of atrial fibrillation, heart electrical activity, multifractal analysis, wavelet transform modulus maxima method,  
29 two-point magnitude correlation analysis, multifractal noise

## 1 INTRODUCTION

30 AF is an arrhythmia originating in the rapid and irregular electrical activity of the atria (the heart's two upper  
31 chambers) that causes their pump function to fail, increasing up to fivefold the risk of embolic stroke (Wolf  
32 et al., 1978, 1991; Attuel et al., 1986; Lip and Lane, 2015). Isolated short episodes of tachy-arrhythmias  
33 may be normal, but if they become more frequent and last longer than one minute then paroxysmal  
34 AF is declared. This condition alone requires treatment of the atrial electrophysiological substrate, all  
35 the more so as AF often coexists with and predisposes to heart failure, with increased morbidity and  
36 mortality (Middlekauff et al., 1991; Stevenson and Stevenson, 1999; Wang et al., 2003). Management of AF  
37 by drug therapy aims at controlling either the ventricular rate, for instance by use of negative chronotropes  
38 such as beta-adrenergic blockers, or the rhythm, by use of anti-arrhythmic drugs interfering with ionic  
39 membrane currents of the excitable cells to prolong the action potential duration (APD), in combination  
40 with anticoagulants, but it does not lead to a cure (Roy et al., 2008; Al-Khatib et al., 2014). Since the  
41 work of Haïssaguerre et al. (Haïssaguerre et al., 1998), radio-frequency ablation of the pulmonary veins  
42 in the left atria has been developed for patients with paroxysmal AF as drug efficacy was found to be  
43 poor or even to become pro-arrhythmic (Echt et al., 1991; The CAST II investigators, 1992). This type of  
44 intervention seeks to punctually destroy sources of abnormal focal electrical activity susceptible to trigger  
45 the arrhythmia. Alternative strategies that have been developed lately include compartmenting the atrium  
46 in order to block possible reentrant circuits, or even directly targeting areas of abnormally fractionated  
47 activity (Nademanee et al., 2004; Camm et al., 2010). Despite the association of various strategies, clinical  
48 efficiency remains disappointing (Ganesan et al., 2013; Takigawa et al., 2014). The rate of AF recurrences  
49 after an initial ablation procedure treating paroxysmal AF increases with time (Bertaglia et al., 2010),  
50 necessitating multiple redos, and most patients suffering persistent AF are resistant to treatment (Camm  
51 et al., 2010; Verma et al., 2015; Wynn et al., 2016).

52 The prevailing electrophysiological concepts describing tachy-arrhythmias are more than a century  
53 old. They involve abnormal automaticity and conduction (Janse, 1997). Initiation and maintenance are  
54 thought to arise from a vulnerable substrate prone to the emergence of multiple self-perpetuating reentry  
55 circuits, also called "multiple wavelets" (Moe and Abildskov, 1959; Moe et al., 1964). Reentries may  
56 be driven structurally, for instance because of locally high fibrous tissue content which badly conducts,  
57 or functionally because of high spatial dispersion of decreased refractoriness and APD (Misier et al.,  
58 1992). The latter is coined the leading circle concept with the clinically more relevant notion of a critical  
59 "wavelength" (in fact the length) of the cardiac impulse (Allessie et al., 1977; Smeets et al., 1986; Rensma  
60 et al., 1988; Attuel et al., 1989). The related concept of vulnerability was originally introduced to uncover  
61 a physiological substrate evolving from normality to pathology. It was found in vulnerable patients that  
62 high rate frequency would invariably lead to functional disorder as cardiac cells would no longer properly  
63 adapt their refractoriness (Attuel et al., 1982). Mathematical models have managed to exhibit likewise  
64 phenomena, with the generation of breaking spiral waves in various conditions (Ito and Glass, 1991; Karma,  
65 1993). The triggering role of abnormal ectopic activity of the pulmonary veins has been demonstrated on  
66 patients with paroxysmal AF resistant to drug therapy (Haïssaguerre et al., 1998), but its origin still remains  
67 poorly understood. This region is highly innervated with sympathetic and parasympathetic stimulation from  
68 the ANS (Tan et al., 2007; Ulphani et al., 2007; Arora, 2012). In particular, Coumel et al. (Coumel et al.,  
69 1978; Coumel, 1994) have revealed the pathophysiological role of the vagal tone on a vulnerable substrate.

70 It is frequently observed that rapid tachycardia of ectopic origin transits to AF. This is known to result from  
71 electrical remodeling. As described for the first time by Allesie et al. (Allesie, 1998), remodeling is a  
72 transient and reversible process by which the impulse properties such as its refractory period are altered  
73 during the course of the arrhythmia, promoting its perpetuation: “AF begets AF” (Wijffels et al., 1995).  
74 Under substantial beating rate increase, cells may undergo remodeling to overcome the toxicity of their  
75 excessive intercellular calcium loading, by a rapid down regulation (a few minutes) of their L-type calcium  
76 membrane current (Yue et al., 1997; Nattel et al., 2008). Moreover, other ionic channel functions are also  
77 modified such as the potassium channel function, inducing a change in the conduction properties including  
78 the conduction velocity (Iwasaki et al., 2011; Nattel and Harada, 2014). The intercellular coupling at the  
79 gap junction level shows also alterations of their connexin expression and dispersion (Severs et al., 2008).  
80 For more details, one may consult Refs (van Marion et al., 2015) and (Zipes et al., 2017).

81 In this study, we delve into the complexity of voltage signals recovered with bipolar electrodes in the CS  
82 during chronic AF. Attempts to assess visually the spatio-temporal complexity of voltage signals using  
83 maps of unipolar electrodes revealed various complex patterns of activity not all compatible with reentries  
84 (Konings et al., 1994, 1997). We use here two declinations of a wavelet-based multi-scale method, the  
85 moment (partition function) method and the magnitude cumulant method (Muzy et al., 1994; Arneodo  
86 et al., 2008), as originally introduced in the field of fully developed turbulence (Muzy et al., 1991). This  
87 methodology has been extensively applied in different domains of fundamental and applied sciences,  
88 including geophysics (Venugopal et al., 2006), econophysics (Muzy et al., 2001), biology (Arneodo et al.,  
89 2011) and medicine (Gerasimova et al., 2014; Gerasimova-Chechkina et al., 2016). In the context of  
90 cardiac physiology, this methodology was shown to be valuable in assessing congestive heart failure from  
91 the monitoring of sinus heart rate variability (Ivanov et al., 1999, 2001; Goldberger et al., 2002). The  
92 wavelet-based multifractal analysis of the electric energy of passing cardiac impulses during AF reported  
93 in the paper provides unprecedented experimental estimates of the multifractal spectra in different heart  
94 areas. The reported results show that the electric energy dynamics looks like a log-normal “multifractal  
95 white noise” with no underlying multiplicative time-scale structure. In a companion paper (Attuel et al.,  
96 2017), we explore the possibility that the substrate function is modulated by the kinetics of conduction. A  
97 simple reversible mechanism of short term remodeling under rapid pacing is demonstrated, by which ionic  
98 overload acts locally (dynamical feedback) on the kinetics of gap junction conductance. The whole process  
99 may propagate and pervade the myocardium via electronic currents. No influence of the ANS is included  
100 and no structural inhomogeneities are taken into account. Then the complete network of excitable cells  
101 becomes desynchronized, with induced dispersion of remodeled refractoriness and APD, and abnormal  
102 automaticity. Contrary to existing mathematical models based on circuit reentries, a spatio-temporal  
103 multifractal intermittent dynamics emerges similar to the one found in the CS next to the left atrial posterior  
104 wall area, opening a new avenue towards the understanding of AF mechanisms of perpetuation.

## 2 METHODS OF ANALYSIS

105 The wavelet transform (WT) is a mathematical microscope (Arneodo et al., 1988, 1995b, 2008; Muzy et al.,  
106 1991, 1994) that is well suited for the analysis of complex non-stationary time-series such as those found in  
107 genomics (Nicolay et al., 2007; Arneodo et al., 2011; Audit et al., 2013) and physiological systems (Ivanov  
108 et al., 1999, 2001; Goldberger et al., 2002; Ciuciu et al., 2012; Chudáček et al., 2014; Gerasimova et al.,  
109 2014; Richard et al., 2015). Thanks to its ability to be blind to non-stationary low-frequency (polynomial)  
110 trends in the analyzed signal  $E(t)$  (or  $E(x)$ ), it has been early recognized as well adapted to reveal the  
111 hierarchy that governs the temporal (or spatial) distribution of singularities of multifractal signals including

112 singular measures and functions (Arneodo et al., 1988; Holschneider, 1988; Jaffard, 1989; Muzy et al.,  
 113 1991; Mallat and Hwang, 1992; Muzy et al., 1994). It is therefore implemented in robust methods capturing  
 114 the self-similar intricate fractal structures hidden in signals that exhibit a typical “1/f noise” scaling as seen  
 115 in the Fourier spectral density (Mandelbrot, 1982, 1998; West and Shlesinger, 1988).

## 116 2.1 The Wavelet Transform Microscope: A Singularity Scanner

117 The WT is a time-scale decomposition method which consists in expanding signals in terms of  
 118 wavelets constructed from a single function, the “analyzing wavelet”  $\psi$ , by means of translations and  
 119 dilations (Grossmann and Morlet, 1984; Daubechies, 1992; Meyer, 1992; Mallat, 1998). The WT of a  
 120 real-valued function  $E$  is defined as:

$$T_\psi[E](t_0, a) = \frac{1}{a} \int_{-\infty}^{+\infty} E(t) \psi\left(\frac{t - t_0}{a}\right) dt, \quad (1)$$

121 where  $t_0$  is a time parameter and  $a$  ( $> 0$ ) a scale parameter (inverse of frequency). By choosing a wavelet  
 122  $\psi$  which has its first  $n_\psi$  moments null [ $\int t^m \psi(t) dt = 0, 0 \leq m < n_\psi$ ], it can be proven that the behavior  
 123 of  $T_\psi[E](t_0, a)$  as a function of the scale  $a$ , as  $a \rightarrow 0^+$ , characterizes the local behavior of  $E(t)$  (Arneodo  
 124 et al., 1988, 1995b, 2008; Jaffard, 1989; Muzy et al., 1991, 1994; Mallat and Hwang, 1992):

$$T_\psi[E](t_0, a) \sim a^{h(t_0)}, \quad a \rightarrow 0^+, \quad (2)$$

125 provided  $n_\psi > h(t_0)$ , where  $h(t_0)$  is the point-wise Hölder exponent that characterizes the maximum  
 126 regularity of the signal  $E$  at point  $t_0$ . If  $n < h(t_0) \leq n + 1$ , the  $(n - 1)$ th derivative of  $E(t)$  is regular  
 127 and its  $n$ th derivative is singular at  $t_0$ . Thus the larger  $h(t_0)$ , the smoother the function, the faster the  
 128 power-law decrease of  $T_\psi[E]$  when  $a \rightarrow 0^+$ . For  $h(t_0) = 0$ ,  $E(t)$  is discontinuous and bounded at  $t_0$   
 129 and the wavelet transform no longer depends on  $a$ . For discontinuous “noise” signals,  $h(t_0) < 0$  and  
 130  $T_\psi[E](t_0, a)$  increases when  $a \rightarrow 0^+$ . For instance,  $h(t_0) = -1$  corresponds to a delta distribution at  $t = t_0$ ,  
 131 while if almost everywhere  $h(t) = -\frac{1}{2}$  the single exponent  $H = \frac{1}{2}$  is characteristic of a “white” noise  
 132 (Muzy et al., 1994). To resolve all the cusp singularities present in a function, the analyzing wavelet must  
 133 be chosen to have enough vanishing moments to resolve the wavelet singularities with Hölder exponent  
 134  $h_{\max}$ , namely  $n_\psi \geq h_{\max}$ . Since  $h_{\max}$  is not known a priori, the most appropriate way to correctly estimate  
 135 all singularities is to analyze the given function with analyzing wavelets of increasing order  $n_\psi$  until a  
 136 robust estimate of the so-called spectrum of singularities is obtained (Bacry et al., 1993; Muzy et al., 1994;  
 137 Arneodo et al., 1995b) (see Sect. 2.2). In the present study, we use the successive derivatives of a Gaussian  
 138 function  $g^{(N)}(t) = \frac{d^N}{dt^N} \left( e^{-t^2/2} \right)$  as analyzing wavelets with  $n_\psi = N$  (Muzy et al., 1994; Arneodo et al.,  
 139 1995b) (Figure S1).

## 140 2.2 A Wavelet-Based Canonical Multifractal Formalism: The Wavelet Transform 141 Modulus Maxima Method

142 The wavelet transform modulus maxima (WTMM) method (Muzy et al., 1991; Bacry et al., 1993;  
 143 Muzy et al., 1994; Arneodo et al., 1995b, 2008) was originally developed to generalize box-counting  
 144 techniques (Arneodo et al., 1987) and to remedy the limitations of structure functions method (Muzy et al.,  
 145 1993) in performing multifractal analysis of one-dimensional (1D) velocity signals in fully-developed  
 146 turbulence. It has proved very efficient to estimate scaling exponents and multifractal spectra (Muzy  
 147 et al., 1994; Audit et al., 2002; Arneodo et al., 2008). From the deep analogy that links the multifractal  
 148 formalism to thermodynamics (Bohr and Tél, 1988; Arneodo et al., 1995b), the WTMM method provides

149 a canonical description (Arneodo et al., 1995b) of the distribution of point-wise Hölder exponents for  
 150 finite  $a$ . The WTMM method allows therefore some control and mastering of finite-size effects and  
 151 statistical convergence issues. As  $a \rightarrow 0^+$ , the thermodynamic limit is reached formally guaranteeing an  
 152 equivalence with micro-canonical approaches such as found in (Turiel et al., 2008). To account for the  
 153 possible presence of oscillating singularities (chirps) (Arneodo et al., 1995a), a grand-canonical multifractal  
 154 formalism has also been developed for signals involving cusp and oscillating singularities (Arneodo  
 155 et al., 1997b). The canonical 1D WTMM method has been generalized in 2D for the multifractal analysis  
 156 of rough surfaces (Arneodo et al., 2000, 2003; Decoster et al., 2000; Roux et al., 2000) and for the  
 157 analysis of 3D scalar and vector fields (Kestener and Arneodo, 2003, 2004; Arneodo et al., 2008) with  
 158 successful applications in astrophysics (Khalil et al., 2006; Kestener et al., 2010; McAteer et al., 2010),  
 159 geophysics (Venugopal et al., 2006; Roux et al., 2009), surface science (Roland et al., 2009), image  
 160 processing (Mallat, 1998; Arneodo et al., 2003, 2008; Antoine et al., 2008), cellular biology (Khalil  
 161 et al., 2007; Snow et al., 2008; Goody et al., 2010; Grant et al., 2010; Martinez-Torres et al., 2014,  
 162 2015) and medicine (Kestener et al., 2001; Arneodo et al., 2003; Khalil et al., 2009; Batchelder et al.,  
 163 2014; Gerasimova-Chechkina et al., 2016; Marin et al., 2017). Note that alternative approaches to the  
 164 WTMM method have been developed using discrete wavelet bases, including the recent use of wavelet  
 165 leaders (Jaffard et al., 2007; Wendt et al., 2007).

### 166 2.2.1 The method of moments

167 In 1D, the WTMM method (Muzy et al., 1991, 1993, 1994; Bacry et al., 1993; Arneodo et al., 1995b)  
 168 consists in computing the WT skeleton defined, at each fixed scale  $a$ , by the local maxima  $\mathcal{L}(a)$  of  
 169 the WT modulus  $|T_\psi[E](t, a)|$ . These WTMM are disposed on curves connected across scales called  
 170 maxima lines (see Figure 2C). Along these maxima lines  $l$ , Mallat and Hwang (Mallat and Hwang, 1992)  
 171 have shown that Eq. (2) also applies for the WTMM that behave as  $|T_\psi[E](t, a)| \sim a^{h(t)}$ , where  $h(t)$  is  
 172 the Hölder exponent characterizing the singularity of the signal  $E$  at time  $t$ . The canonical multifractal  
 173 formalism (Muzy et al., 1994; Arneodo et al., 1995b) characterizes the relative contributions of each  
 174 Hölder exponent value via the estimate of the singularity spectrum  $D(h)$  defined as the fractal (Hausdorff)  
 175 dimension of the set of points  $t$  where  $h(t) = h$ . This spectrum can be obtained by investigating the scaling  
 176 behavior of partition functions defined in terms of WTMM (and which correspond to the moments of the  
 177 WTMM probability distribution function):

$$Z(q, a) = \sum_{l \in \mathcal{L}(a)} |T_\psi[E](t, a)|^q \sim a^{\tau(q)}, \quad a \rightarrow 0^+, \quad (3)$$

178 where  $q \in \mathbb{R}$ , and  $\mathcal{L}(a)$  is the set of all maxima lines  $l$  that satisfy:  $l \in \mathcal{L}(a)$ , if  $\forall a' \leq a, \exists (t, a') \in l$ . In the  
 179 framework of the analogy with thermodynamics (Bohr and Tél, 1988; Arneodo et al., 1995b),  $q$  and  $\tau(q)$   
 180 play respectively the role of an inverse temperature and a free energy. The main result of the canonical  
 181 wavelet-based multifractal formalism is that in place of energy and entropy (*i.e.* the variables conjugated  
 182 to  $q$  and  $\tau$ ), we have  $h$ , the Hölder exponent, and  $D(h)$ , the singularity spectrum. This means that the  
 183 singularity spectrum of  $E(t)$  is a convex function that can be calculated from the Legendre transform of  
 184 the partition function scaling exponents  $\tau(q)$  (Bacry et al., 1993; Muzy et al., 1993, 1994; Arneodo et al.,  
 185 1995b):

$$D(h) = \min_q [qh - \tau(q)]. \quad (4)$$



186 In practice, to avoid instabilities in performing the Legendre transform, we instead compute the following  
 187 expectation values (Muzy et al., 1994; Arneodo et al., 1995b), analogous to the fundamental thermodynamic  
 188 relations, by inversion of Eq. (4):

$$h(q, a) = \frac{\partial}{\partial q} \ln(Z(q, a)) = \sum_{l \in \mathcal{L}(a)} \ln(|T_\psi[E](t, a)|) \cdot W_\psi[E](q, l, a), \quad (5)$$

189 and

$$D(q, a) = q \frac{\partial}{\partial q} \ln(Z(q, a)) - \ln(Z(q, a)) = \sum_{l \in \mathcal{L}(a)} W_\psi[E](q, l, a) \cdot \ln(W_\psi[E](q, l, a)), \quad (6)$$

190 where  $W_\psi[E](q, l, a) = |T_\psi[E](t, a)|^q / Z(q, a)$  corresponds to the Boltzmann weight in the analogy that  
 191 connects the multifractal formalism to thermodynamics (Arneodo et al., 1995b). Then, from the slopes of  
 192  $h(q, a)$  and  $D(q, a)$  versus  $\ln a$ , we get  $h(q)$  and  $D(q)$ , and therefore the  $D(h)$  singularity spectrum as a  
 193 curve parametrized by  $q$ . For further mathematical developments on the 1D WTMM method, we refer the  
 194 reader to Bacry et al. (Bacry et al., 1993) and Jaffard (Jaffard, 1997a,b).

### 195 2.2.2 The method of magnitude cumulants

196 With the previous method of moments, to compute the entire  $\tau(q)$  curve, we need to perform linear  
 197 regression fits of  $\ln Z(q, a)$  vs  $\ln a$  (Eq. (3)) for a wide range of  $q$  values and then to proceed to a polynomial  
 198 fit of the  $\tau(q)$  data prior to the Legendre transform (Eq. (4)) to get the  $D(h)$  singularity spectrum. An  
 199 alternative method based on magnitude cumulants has been introduced by Delour et al. (Delour et al., 2001)  
 200 to minimize the number of linear regression fits (as few as 3) while still adequately inferring and accurately  
 201 estimating the nonlinear behavior of the  $\tau(q)$  spectrum. This method is based on the following reasoning.  
 202 The computation of the partition function  $Z(q, a)$  amounts to computing the following arithmetic mean of  
 203 the WTMM to the power  $q$ :

$$\langle |T_a|^q \rangle = \frac{1}{N_a} Z(q, a), \quad (7)$$

204 where we simplified notations  $T_a \equiv T_\psi[E](\cdot, a)$ , and where  $N_a$  is the number of maxima lines at scale  $a$ ,  
 205 which scales as  $\sim a^{-D_f}$ , where  $D_f = -\tau(0)$  is the fractal dimension of the support set of the singularities  
 206 in the signal  $E(t)$ . From Eqs. (3) and (7), we get the expansion

$$\begin{aligned} [\tau(q) + D_f] \ln a &\sim \ln\{e^{q \ln |T_a|}\}, \\ &\sim \sum_{n=1}^{\infty} C_n(a) \frac{q^n}{n!}, \end{aligned} \quad (8)$$

207 where  $C_n(a)$  are the cumulants of the magnitude  $\ln |T_a|$ . Then from the behavior of these cumulants:

$$\begin{aligned} C_1(a) &\equiv \langle \ln |T_a| \rangle \sim c_1 \ln(a), \\ C_2(a) &\equiv \langle \ln^2 |T_a| \rangle - \langle \ln |T_a| \rangle^2 \sim -c_2 \ln a, \\ C_3(a) &\equiv \langle \ln^3 |T_a| \rangle - 3\langle \ln^2 |T_a| \rangle + 2\langle \ln |T_a| \rangle^3 \sim c_3 \ln a, \\ &\dots \end{aligned} \quad (9)$$

208 we get the following expansion formula for  $\tau(q)$ :

$$\begin{aligned} \tau(q) &= -D_f \frac{q^0}{0!} + \sum_{n=1}^{\infty} \left[ \frac{C_n(a)}{\ln a} \right] \frac{q^n}{n!}, \\ &= -c_0 + c_1 q - c_2 q^2/2! + c_3 q^3/3! \dots \end{aligned} \tag{10}$$

209 where the coefficients  $c_n > 0$  are estimated as the slope of  $C_n(a)$  vs  $\ln a$  ( $n = 1, 2, 3, \dots$ ), and  
210  $c_0 = D_f$ .

211 The implication of the above developments is that we can estimate  $\tau(q)$  from the polynomial expansion  
212 of Eq. (10), where the coefficients are obtained from the log-log linear regressions of the cumulants of  
213 the magnitude  $C_n(a)$  vs  $\ln(a)$  (Eq. (9)) (Delour et al., 2001). A quadratic log-normal  $\tau(q)$  approximation  
214 would need only three such linear regressions,  $c_n = 0, \forall n > 2$ .

### 215 2.3 Monofractal versus multifractal functions

216 Homogeneous monofractal signals (distributions) are signals with singularities of unique Hölder exponent  
217  $H$ . Their  $\tau(q)$  spectrum is a linear function of  $q$  with slope  $c_1 = H$  (Eq. (9)). Monofractal scaling indeed  
218 means that the shape of the probability distribution function (pdf) of rescaled wavelet coefficients does  
219 not change across scales as expressed by the following relationship between the WTMM pdfs  $P_a(T)$  and  
220  $P_{a'}(T)$  at scale  $a$  and  $a' > a$  respectively (Arneodo et al., 2002, 2011):

$$P_a(T) = \left(\frac{a'}{a}\right)^{-H} P_{a'}\left(\left(\frac{a'}{a}\right)^{-H} T\right). \tag{11}$$

221 A nonlinear  $\tau(q)$  is the signature of multifractal signals with Hölder exponent  $h(t)$  fluctuating over time  
222  $t$  (Muzy et al., 1991, 1994; Bacry et al., 1993; Arneodo et al., 1995b, 2002, 2008). In this study, we  
223 fit the  $\tau(q)$  data by the so-called log-normal quadratic approximation  $\tau(q) = -c_0 + c_1 q - c_2 q^2/2$ . The  
224 corresponding singularity spectrum has a quadratic single humped shape:

$$D(h) = c_0 - (h - c_1)^2/2c_2, \tag{12}$$

225 where  $c_0 = -\tau(0) = D_f$  is the fractal dimension of the support of singularities of  $E(t)$ ,  $c_1$  is the value of  
226  $h$  that maximizes  $D(h)$ , and the intermittency coefficient  $c_2$  (Delour et al., 2001) characterizes the width  
227 of the  $D(h)$  spectrum as an indication of a change in WTMM coefficient statistics across scales. If  $h(t)$   
228 fluctuates according to a pdf  $\rho(h)$ , then (Castaing et al., 1990, 1993; Arneodo et al., 1997a, 1998c, 1999):

$$P_a(T) = \int \rho(h) \left(\frac{a'}{a}\right)^{-h} P_{a'}\left(\left(\frac{a'}{a}\right)^{-h} T\right) dh, \tag{13}$$

229 meaning that the pdf at scale  $a$  can be expressed as a weighted sum of dilated pdfs at larger scales  $a' > a$ .  
230 Let us point out that the monofractal situation (Eq. (11)) is recovered when assuming that  $\rho(h) = \delta(h - H)$   
231 in Eq. (13).

232 Note that  $\tau(2) = c_0 + 2c_1 - 2c_2$ , also called the correlation dimension, is related to the “1/f” scaling  
233 exponent of the Fourier spectral density (Muzy et al., 1994; Mandelbrot, 1998):

$$|\widehat{E}(f)|^2 \sim f^{-\beta}, \text{ with } \tau(2) = \beta - 2. \tag{14}$$



## 234 2.4 In Quest of an Underlying Time-Scale Multiplicative Structure: The Two-Points 235 Magnitude Correlation Method

236 Multiplicative cascade processes (Arneodo et al., 1998b) are paradigmatic mechanisms generating  
237 multifractal distributions, with as historical examples the Kolmogorov–Obukhov log-normal energy cascade  
238 model of fully developed turbulence (Kolmogorov, 1962; Oboukhov, 1962; Mandelbrot, 1974), and the  
239 Multifractal Random Walk (MRW) model recently introduced to account for the intermittency observed  
240 in financial time series (Muzy et al., 2000; Bacry et al., 2001). But, if multifractal scaling implies some  
241 evolution of the WTMM statistics across scales, it does however not require any correlation of the wavelet  
242 coefficients across scales. In addition to the above one-point WTMM statistics, it is thus useful to study the  
243 two-point correlation function of the logs of the WTMM coefficients  $\ln |T_a(t)|$ , which determines the way  
244 the correlation structure of the Hölder exponents  $h$  (or singularities) changes with scale (Arneodo et al.,  
245 1998a,b). Defining the two-point magnitude correlation function  $C(a, \Delta t)$  as:

$$C(a, \Delta t) = \langle (\ln |T_a(t)| - \langle \ln |T_a(t)| \rangle) \cdot (\ln |T_a(t + \Delta t)| - \langle \ln |T_a(t)| \rangle) \rangle, \quad (15)$$

246 and seeing how this correlation changes as a function of  $\Delta t$  at scale  $a$ , provides information about the  
247 time-scale structure that underlies the multifractal properties of the considered signal. As demonstrated by  
248 Arneodo et. al. (Arneodo et al., 1998a,b) for random multiplicative cascades on wavelet dyadic trees (see  
249 also (Meneveau and Sreenivasan, 1991)):

$$C(a, \Delta t) \sim -c_2 \ln \Delta t, \quad \Delta t > a, \quad (16)$$

250 where the proportionality coefficient  $c_2$  is the intermittency coefficient defined in Eq. (9) (Note that  
251  $C(a, \Delta t = 0) \equiv C_2(a) \sim -c_2 \ln a$ ). Thus, by computing  $C(a, \Delta t)$  from Eq. (15) and plotting it  
252 as a function of  $\ln \Delta t$ , inferences can be made about long-range dependence and consistency with a  
253 multiplicative cascading process (Arneodo et al., 1998a,b). Applications of the two-point magnitude  
254 correlation method have already provided insight into a wide variety of problems, *e.g.* the validation of the  
255 log-normal cascade phenomenology of fully developed turbulence (Arneodo et al., 1998a,c, 1999) and of  
256 high resolution temporal rainfall (Venugopal et al., 2006; Roux et al., 2009), and the demonstration of the  
257 existence of a causal cascade of information from large to small scales in financial time series (Arneodo  
258 et al., 1998d; Muzy et al., 2001).

## 3 DESCRIPTION OF DATA

### 259 3.1 Study design and population

260 The experimental data are hospital-based. We have analyzed data recorded in the atria of 8 patients with  
261 persistent or chronic AF, chosen without any prior explicit exclusion criteria. These patients were enrolled  
262 to undergo radio frequency ablation between 2010 and 2012, in the international cardiac electrophysiology  
263 service of public hospital CHU Haut-Lévêque in Pessac, France. All patients gave written informed consent  
264 to the investigation of data from the intervention. A protocol for clinic research was approved by the  
265 institutional Clinical Research and Ethics Committee. For this specific investigation of the data, the authors  
266 accessed fully anonymized and de-identified data. As representative of the results obtained with our set of  
267 patients, we report in this manuscript the results of a detailed wavelet-based multifractal analysis of five  
268 long time series specially recorded in one of the 8 patients with chronic AF.

## 269 3.2 Electric Potential Recording

270 A steerable decapolar catheter, equipped with five 1 mm distant pairs of electrodes, each pair separated by  
 271 5 mm (Xtrem, Sorin Medical ©), was positioned in the CS as recommended in guidelines (Figures 1A,B).  
 272 The distal leads of the catheter tip are positioned in a region near the left pulmonary veins, while the  
 273 proximal leads lie closer to the right atrium orifice of the CS. This catheter was immobile and probed  
 274 the electrical activity of those areas in the left atrium. Monitoring typically lasted the whole intervention  
 275 which could take hours. Our file consists of 5 simultaneous recordings at points Pt1 to Pt5, from distal to  
 276 proximal positioning along the vein (Figure 1A), each lasting 422 seconds with sampling time  $10^{-3}$  s, a  
 277 few minutes before the first ablation procedure started. The potential difference  $\Delta\phi(t)$  between each of  
 278 the two electrodes in each pair was recorded, with the convention of distal minus proximal (Figure 1C).  
 279 The normal to rapid frequency in sinus rhythm varies in the range  $1\text{Hz} \lesssim f \lesssim 3\text{Hz}$ , whereas during AF it  
 280 is typically in the range  $3\text{Hz} \lesssim f \lesssim 10\text{Hz}$  (Figure 1D). But the most obvious observation is that on-site  
 281 recordings during AF contrast with the ones during sinus rhythm as the former seem to fluctuate randomly  
 282 at even higher frequencies. Physiologically, a natural high frequency cut-off is somewhere in between  
 283  $100\text{Hz} \lesssim f_c \lesssim 1000\text{Hz}$ , which corresponds to the shortest characteristic time scale in a cardiac cell cycle,  
 284 that is depolarization. Furthermore, AF is considered as the most irregular cardiac arrhythmia (Konings  
 285 et al., 1994, 1997).

## 286 3.3 Local Impulse Energy

287 Each electrode averages the electric potential over its surface. During depolarization, ions flow through  
 288 the cell membrane channels and the gap junction channels, inducing a rapid change of the electric potential  
 289 ( $\sim 10^{-2}$ s). Then, repolarization is a much smoother event. Bipolar electrodes are separated by one or  
 290 two millimeters which is typically the length scale of a depolarizing front in the atria with a conduction  
 291 velocity  $c \sim 10^{-2}$  m/s and a refractory period  $RP \sim 10^{-1}$  s (Figures S2A,B), thus defining the so-called  
 292 “wavelength” scale  $c \times RP$  (Smeets et al., 1986; Rensma et al., 1988). Any spatio-temporal variation of  
 293 the vulnerable substrate function happens over larger time scales. Thus the conduction velocity can be  
 294 considered constant over such small scales and the bipolar electric potential difference is therefore “frozen”.  
 295 It follows that the bipolar electric potential difference is locally advected with velocity  $c$ :

$$\frac{\partial \Delta\phi(t)}{\partial t} = -c \vec{\nabla} \Delta\phi(t). \quad (17)$$

296 Under this assumption, the evaluation of the local electric energy of a cardiac impulse is straight-forward:

$$\frac{\varepsilon}{2} \mathcal{E}^2(t) = \frac{\varepsilon}{2c^2} \left( \frac{\partial}{\partial t} \Delta\phi(t) \right)^2, \quad (18)$$

297 where  $\mathcal{E}$  is the electric field magnitude and  $\varepsilon$  is the dielectric bulk permittivity of the (inter-) cellular medium.  
 298 Energy will thus peak when the impulse travels between the two electrodes. It fully incorporates ionic flux  
 299 through membrane channels and electrotonic currents, specifically those taking place at the gap junctions.  
 300 Because we have no means to assess the conduction velocity  $c$ , we will use in this study the following  
 301 definition of the energy:

$$E(t) = \left( \frac{\partial \Delta\phi(t)}{\partial t} \right)^2, \quad (19)$$

302 after dropping the term in front of the r.h.s. of Eq. (18), *i.e.*  $\varepsilon/2c^2$  which remains constant at first order as  
 303 long as the conduction velocity  $c$  does not fluctuate too much. To practically derive  $E(t)$  from the recorded  
 304  $\Delta\phi(t)$ , we used an order 4 finite difference scheme on a oversampled ( $\Delta t_0 = 10^{-4}$ s) cubic-spline fitting  
 305 of the data (Figures S2C,D). This is needed to estimate peaks in the energy within temporal windows as  
 306 narrow as  $\sim 10^{-3}$  s (Figures S2E,F). We have checked that the scaling properties displayed by  $E(t)$  in the  
 307 low frequency range of interest here ( $0.08\text{Hz} \lesssim f \lesssim 2\text{Hz}$ ) are not affected by this discretization scheme.

308 Let us note that Eq. (19) is not without reminding the 1D surrogate dissipation approximation  $E_{\text{dis}}(t) \sim$   
 309  $(\partial v/\partial t)^2$ , where  $v$  is the longitudinal velocity, in fully developed (homogeneous and isotropic) turbulence  
 310 under the Taylor hypothesis of “frozen” turbulence (Meneveau and Sreenivasan, 1991; Frisch, 1995).

### 311 3.4 Software and Documentation

312 The numerical procedure to perform the WTMM analysis of 1D signals can be downloaded at

313 <http://perso.ens-lyon.fr/benjamin.audit/LastWave>

314 LastWave is open source software written in C. We recommend interested users to read the LastWave  
 315 C-Application Programming Interface documentation and to contact the corresponding author to be directed  
 316 to the part of the code of most relevance to them.

## 4 RESULTS

### 317 4.1 One-Point Multifractal Analysis of Local Impulse Energy Data

318 We first present an exhaustive step-by-step analysis of one of the impulse energy time-series recorded at  
 319 the electrode Pt2 as an illustration of the intricacies involved in the methodology and as a demonstration  
 320 that without a priori knowledge about the signal, a reliable multifractal analysis requires an iterative process  
 321 between diagnosis and estimation until robustness is achieved. In Figure S3 is illustrated how the WT  
 322 microscope is able to filter out the nonstationarities (polynomial trends) in  $E(t)$  (Figure S3A) when using  
 323 analyzing wavelets  $g^{(N)}$  (Figure S1) of increasing order (Figures S3B,C,D).

#### 324 4.1.1 Multifractal analysis of the impulse energy data with the WTMM method of moments

325 When applying the WTMM method to the impulse energy time-series recorded at Pt2 (Figure 2A), we  
 326 revealed that the partition functions  $Z(q, a)$  (Eq. (3)) obtained from the WT computed with the analyzing  
 327 wavelet  $g^{(3)}$  (Figure 2B) and its skeleton (Figure 2C), display nice scaling properties for  $q = -1$  to 5 over a  
 328 range of time-scales larger than the mean interbeat  $\sim 0.5$  s (Figure 1D). We strictly limited this range to (0.6,  
 329 10 s) for linear regression fit estimates in a logarithmic representation (Figure 3A). The  $\tau(q)$  so-obtained is  
 330 well approximated by a quadratic spectrum with parameters  $[c_0, c_1, c_2] = [1.01, -0.34, 0.053]$  and  $c_n = 0$   
 331 for  $n > 2$  (Eq. (10)) (Figure 4A). This signature of multifractality with a support of singularities of fractal  
 332 dimension  $D_f \approx 1$ , and an intermittency coefficient  $c_2 = 0.053 \pm 0.010$  (Table 1) is confirmed when  
 333 respectively plotting  $h(q, a)/\ln 2$  (Eq. (5)) and  $D(q, a)/\ln 2$  (Eq. (6)) vs  $\log_2 a$  in Figures 3B,C. From  
 334 the estimate of the slopes  $h(q)$  and  $D(q)$ , we get the single humped  $D(h)$  spectrum shown in Figure 4B  
 335 which is well approximated by the quadratic spectrum defined in Eq. (12) with the above parameter values  
 336 obtained from a polynomial fitting of the  $\tau(q)$  data. Interestingly, when comparing the results obtained with  
 337 the analyzing wavelet  $g^{(3)}$  with those obtained with  $g^{(1)}$  and  $g^{(2)}$  in Figures 3 and 4, we notice that except  
 338 some slight differences observed when using the first-order analyzing wavelet  $g^{(1)}$ , the multifractal spectra

339 obtained with the second-order wavelet  $g^{(2)}$  and the third-order wavelet  $g^{(3)}$  almost superimpose (Figure 4,  
340 Table 1) with singularities of Hölder exponent  $h \leq 0$ , characteristic of a multifractal “noise” signal.

341 This multifractal diagnosis is confirmed in Figure 5 where the WTMM pdfs obtained at different scales  
342 with  $g^{(3)}$  (Figure 5A) are shown to collapse on each other when using the propagative equation of the  
343 statistics across scales (Eq. (13)) with the quadratic  $\tau(q)$  spectrum estimated just above (Figure 5B)  
344 (Castaing et al., 1990, 1993; Arneodo et al., 1997a, 1998c, 1999; Venugopal et al., 2006).

#### 345 4.1.2 Multifractal analysis of the impulse energy data with the method of magnitude cumulants

346 After the WTMM partition function approach, we turn our attention to the alternate magnitude cumulant  
347 analysis methodology. The first-, second- and third-order cumulants were computed using Eq. (9) and are  
348 plotted versus the logarithm of the scale in Figure 6. As expected  $C_1(a)$ ,  $C_2(a)$  and  $C_3(a)$  display consistent  
349 scaling behavior over the same range of scales  $2^9 \leq a \leq 2^{13}$  ( $a = \Delta t / \Delta t_0$ , where the oversampling time  
350 is  $\Delta t_0 = 10^{-4}$  s) and this for the three analyzing wavelets  $g^{(1)}$ ,  $g^{(2)}$  and  $g^{(3)}$ . The results obtained for  
351  $C_3(a)$  (Figure 6C) confirm that with the limited statistical sample at our disposal (422 s long time series),  
352 there is no way to conclude about the possible departure from a log-normal quadratic  $\tau(q)$  spectrum ( $c_3 \equiv$   
353 0). Nicely, the quadratic  $\tau(q)$  spectrum obtained with  $g^{(3)}$  with parameters  $c_1^* = -0.33 \pm 0.01$  and  
354  $c_2^* = 0.047 \pm 0.028$  is found in good agreement with the one previously estimated with the method of  
355 moments, confirming the multifractal diagnosis of the local impulse energy at low frequencies. Let us point  
356 out that, as reported in Table 1, the  $\tau(q)$  spectrum obtained with  $g^{(1)}$  is again slightly different from the  
357 ones obtained with  $g^{(2)}$  and  $g^{(3)}$  which turn out to be indistinguishable. This is the numerical demonstration  
358 that a robust estimate of the multifractal spectra is achieved when using the third-order analyzing wavelet  
359  $g^{(3)}$ .

#### 360 4.1.3 Summary of one-point multifractal analysis of the impulse energy data

361 Similar analysis was performed on the four other local impulse energy time-series recorded at electrodes  
362 Pt1 (Figures S4, S8 and S11), Pt3 (Figures S5, S9, S12), Pt4 (Figures S6, S13), and Pt5 (Figures S7, S10,  
363 S14). As already noticeable on the power spectrum in Figure 1D, the electric potential  $\Delta\phi(t)$  recorded at  
364 electrode Pt4 presents some subharmonic oscillatory component at frequency  $\sim 2.5$  Hz that dramatically  
365 spoils the scaling behavior previously obtained at Pt2 over the range of time-scales (0.6, 10 s) (Figures S6,  
366 S13). We can speculate on the signature of the nearby mitral valve influence. This explains that Pt4 will  
367 be singled out in the rest of our study. Figure 7 displays the  $\tau(q)$  (Figure 7A) and  $D(h)$  (Figure 7B)  
368 spectra of the local impulse energy  $E(t)$  obtained with the WTMM method of moments when using  
369 the analyzing wavelet  $g^{(3)}$  (the corresponding spectra obtained with analyzing wavelets  $g^{(1)}$  and  $g^{(2)}$  are  
370 shown in Figures S15 and S16 respectively). The spectra obtained for the time-series recorded at electrode  
371 Pt1 situated, as Pt2, in the ligament of Marshall anatomic area innervated by the ANS (Figure 1A), are  
372 very similar to the ones observed at Pt2. Both  $\tau(q)$  and  $D(h)$  spectra are well approximated by quadratic  
373 spectra (Eqs. (9) and (10) respectively) with parameters  $[c_0, c_1, c_2] = [1.01, -0.28, 0.064]$  (Figure 7) with  
374 a definitely positive finite intermittency coefficient  $c_2 = 0.064 \pm 0.014$  (Table 1). Interestingly, time  
375 series recorded at electrodes Pt3 and Pt5 in a different anatomical area next to the left atrial posterior  
376 wall (Figure 1A) both show rather similar  $\tau(q)$  and  $D(h)$  multifractal spectra but significantly different  
377 from the ones obtained at electrodes Pt1 and Pt2 (Figure 7). Again these spectra are found nearly quadratic  
378 with parameters  $[c_0, c_1, c_2] = [1.02, -0.48, 0.098]$  for Pt3, and  $[1.03, -0.38, 0.152]$  for Pt5 (Table 1). Local  
379 impulse energy time series at Pt3 and Pt5 show higher intermittency with larger  $c_2$  values whereas they  
380 display weaker long-range correlations  $c_1 = \langle h \rangle \sim -0.45$  (i.e. closer to  $c_1 = -0.5$  a value characteristic  
381 of uncorrelated white noise), instead of the value  $c_1 \sim -0.3$  for Pt1 and Pt2 characteristic of positive

382 long-range correlations. As reported in Table 1, this regionalization of the multifractal properties of  
 383 the local impulse energy is quantitatively confirmed when using the magnitude cumulant method. It  
 384 is further corroborated when reproducing this multifractal analysis for other patients with paroxysmal,  
 385 persistent or chronic AF (Figure 8A) and for a patient at different periods of time preceding ablation  
 386 procedure (Figure 8B) as an indication of stationarity.

## 387 4.2 Two-Point Magnitude Analysis of Local Impulse Energy Data

388 The results of the two-point magnitude correlation analysis of the local impulse energy time series  
 389 recorded at the positions Pt1, Pt2, Pt3 and Pt5 along the CS vein are shown in Figure 9.  $C(a, \Delta t)$  (Eq. (15))  
 390 computed with the analyzing wavelet  $g^{(3)}$  is represented versus  $\Delta t$  for two scales  $a = 2^9$  and  $2^{10}$  in the  
 391 scaling range. Strikingly for all four time series, for  $\Delta t \gtrsim a$ ,  $C(a, \Delta t)$  drops to zero as a clear indication  
 392 that the magnitudes are uncorrelated. As a reference, we put in each panel of Figure 9, a dashed straight  
 393 line of slope  $-c_2$  as predicted by Eq. (16) for multifractal signals exhibiting a cascading multiplicative  
 394 structure along a time-scale tree (Arneodo et al., 1998b). The slow decay predicted by the “multiplicative”  
 395 log-normal model with intermittency coefficient  $c_2$  is definitely not observed. Thus, local impulse energy  
 396 time-series look much more like what has been called log-normal “mutlifractal white noise” in pioneering  
 397 works to distinguish “uncorrelated” and “multiplicative” log-normal models (Arneodo et al., 1998a). A  
 398 similar absence of magnitude correlation is observed when reproducing this two-point magnitude analysis  
 399 with the analyzing wavelets  $g^{(1)}$  (Figure S17) and  $g^{(2)}$  (figure S18).

## 5 DISCUSSION

400 To summarize, we showed that the wavelet-based multifractal analysis of long time series of the local  
 401 impulse energy recorded in the CS of a patient with chronic AF was able to reveal and quantify the  
 402 intermittent nature of these signals at low frequency ( $f \lesssim 2$  Hz). To our knowledge, our study is the  
 403 first to report on the observation and quantification of such multifractal dynamics of the endocavitary  
 404 electrical activity during chronic AF which is found more complex than previously suspected. On the basis  
 405 of the analysis of the time-series recorded at 4 catheter electrodes out of 5 positioned in the CS, two main  
 406 observations can be made: (i) the local impulse energy displays different multifractal properties in the  
 407 left atrial wall area than in the ligament of Marshall area consistently with different anatomical substrate  
 408 conditions, and (ii) while recorded along the CS vein, the local impulse energy does not exhibit long-  
 409 range dependence associated with an underlying multiplicative cascade, or in other words the multifractal  
 410 distribution of the singularities inferred by the two-point magnitude analysis does not display any correlation  
 411 across scales just like a log-normal “multifractal white noise” (Arneodo et al., 1998a). The nature of this  
 412 study was exploratory, with a data set limited to a few patients, and with a few time series rather long for  
 413 clinical practice (422 s) but not so long regarding the range of time scales [0.6, 10 s] where scaling was  
 414 observed. This is the reason for the different complementary analyses employed in this paper including the  
 415 WTMM method of moments, the WTMM method of magnitude cumulants, and the two-points magnitude  
 416 cumulant method, using analyzing wavelets of different orders, until reliable estimates were obtained. Of  
 417 course our results deserve to be confirmed over a large set of patients at different stages of AF development  
 418 and be explored in different areas of the atria. But this preliminary analysis definitely challenges current  
 419 knowledge in physical, physiological and clinical fundamentals of AF arrhythmia.

420 The absence of an underlying cascading process is not such a surprise since underlying the multifractal  
 421 properties displayed by the local impulse energy at low frequencies ( $f \lesssim 2$  Hz), there is no clear 3D  
 422 “fragmentation” (Mandelbrot, 1982) process inducing some cascading of energy from large to small time

423 scales and also no obvious 2D “aggregation, coalescence or growth” (Vicsek, 1989) process bringing  
424 energy from small to large time scales. What are the physical and physiological mechanisms that drive  
425 the multifractal nature of local impulse energy and give rise to the observed differences according to area  
426 is still an open question. Nonetheless, these results already undermine the commonly accepted concepts  
427 revolving around circuit reentries, and a fortiori spiral waves, as being basic mechanisms for the onset  
428 and perpetuation of AF. The mechanistic “wavelength” criterion indeed conveys the idea that random  
429 spatio-temporal dispersion of refractoriness, or more generally of functional properties, leads to random  
430 mixing of circuit reentries. The “wavelength” scale adjusts naturally to the typical scale  $\lambda$  of dispersion  
431 when it exists  $c \times RP \lesssim \lambda$ , as would be the case for Gaussian statistics of dispersion. In that case, the  
432 statistics of the local impulse energy remains Gaussian throughout scales. On the contrary, to fit our new  
433 observations we have seen that the statistics is not Gaussian and evolves across scales through a log-normal  
434 propagation law which accounts for the intermittency observed over the range of a few beat cycles ( $\sim 0.6$  s)  
435 to several tens ( $\sim 10$  s) (and possibly more), therefore spanning the whole atria. Although the ligament  
436 of Marshall area is highly innervated (Tan et al., 2007; Ulphani et al., 2007; Arora, 2012), it is quite  
437 unlikely that modulations by the ANS, that affects heart rate, play a significant role in the intermittent  
438 dynamics since the documented three peak frequencies at  $\sim 0.4$  Hz,  $\sim 0.15$  Hz and  $\sim 0.04$  Hz (Akselrod  
439 et al., 1981) do not show up in our analysis. Furthermore, we have found at least two areas with different  
440 multifractal regimes. Thus, our findings raise new challenging questions calling for ongoing efforts to  
441 develop physiological heart tissue models that account for the low frequency intermittent nature of local  
442 impulse energy. Recent studies in animal models suggest the protective role of connexin gene transfer to  
443 prevent sustained AF (Bikou et al., 2011; Igarashi et al., 2012). In this spirit, in a companion modeling  
444 paper (Attuel et al., 2017), we propose a model of gap junction conduction remodeling in a denervated heart  
445 that accounts for the observed intermittent dynamics over large time scales, as resulting from incoherent  
446 random back scatterings leading to the desynchronization of the network of cardiac excitable cells.

## AUTHOR CONTRIBUTIONS

447 **Conception and design:** GA, HY, AA.  
448 **Development and methodology:** EGC, FA, AA.  
449 **Analysis and interpretation of data:** GA, EGC, FA, HY, AA.  
450 **Acquisition of data (provided animals, acquired and managed patients, provided facilities, etc.):** GA,  
451 HY.  
452 **Writing, review, and/or revision of the manuscript:** GA, EGC, FA, HY, AA.  
453 **Administrative, technical or material support (i.e. requiring and organizing data, constructing**  
454 **databases):** GA, EGC.  
455

## FUNDING

456 This work was partially supported by Contrat Conseil Région Aquitaine CAVERNOM “Cardiac Arrhythmia  
457 Complexity and Variability by means of Robust Nonlinear Methods” (Grant N° 2014-1R60212-00003295),  
458 by the President of Russian for the young scientists (Grant N° 14.W01.17.2674-MK), and by the Metchnikov  
459 Program (EGC visit to LOMA).



## ACKNOWLEDGEMENTS

460 The data used in this study have been provided by IHU Liryc, Hôpital Xavier Arnoz, Avenue du Haut  
461 Lévêque, 33604 Pessac cedex.

## SUPPLEMENTAL DATA

462 The supplementary Material for this article can be found online at...

## REFERENCES

- 463 Akselrod, S., Gordon, D., Ubel, F. A., Shannon, D. C., Barger, A. C., and Cohen, R. J. (1981). Power  
464 spectrum analysis of heart rate fluctuations : A quantitative probe of beat-to-beat cardiovascular control.  
465 *Science* 213, 220–222
- 466 Al-Khatib, S. M., LaPointe, N. M. A., Chatterjee, R., Crowley, M. J., Dupre, M. E., Kong, D. F., et al.  
467 (2014). Rate-and rhythm-control therapies in patients with atrial fibrillation: A systematic review. *Ann.*  
468 *Int. Med.* 160, 760–773
- 469 Allessie, M. A. (1998). Atrial electrophysiologic remodeling : another vicious circle ? *J. Cardiovasc.*  
470 *Electrophysiol.* 9, 1378–93
- 471 Allessie, M. A., Bonke, F. I., and Schopman, F. J. (1977). Circus movement in rabbit atrial muscle as a  
472 mechanism of tachycardia. *Circ. Res.* 41, 9–18
- 473 Antoine, J. P., Murenzi, R., Vanderghenst, P., and Ali, S. T. (2008). *Two-Dimensional Wavelets and their*  
474 *Relatives* (Cambridge: Cambridge University Press)
- 475 Arneodo, A., Audit, B., Decoster, N., Muzy, J.-F., and Vaillant, C. (2002). A wavelet based multifractal  
476 formalism: Application to DNA sequences, satellite images of the cloud structure and stock market data.  
477 In *The Science of Disasters: Climate Disruptions, Heart Attacks, and Market Crashes*, eds. A. Bunde,  
478 J. Kropp, and H. J. Schellnhuber (Berlin: Springer Verlag). 26–102
- 479 Arneodo, A., Audit, B., Kestener, P., and Roux, S. G. (2008). Wavelet-based multifractal analysis.  
480 *Scholarpedia* 3, 4103
- 481 Arneodo, A., Bacry, E., Jaffard, S., and Muzy, J.-F. (1997a). Experimental analysis of self-similarity and  
482 random cascade processes: Application to fully developed turbulence data. *J. Phys. II* 7, 363–370
- 483 Arneodo, A., Bacry, E., Jaffard, S., and Muzy, J.-F. (1997b). Oscillating singularities on Cantor sets: a  
484 grand-canonical multifractal formalism. *J. Stat. Phys.* 87, 179–209
- 485 Arneodo, A., Bacry, E., Manneville, S., and Muzy, J.-F. (1998a). Analysis of random cascades using  
486 space-scale correlation functions. *Phys. Rev. Lett.* 80, 708–711
- 487 Arneodo, A., Bacry, E., and Muzy, J.-F. (1995a). Oscillating singularities in locally self-similar functions.  
488 *Phys. Rev. Lett.* 74, 4823–4826
- 489 Arneodo, A., Bacry, E., and Muzy, J.-F. (1995b). The thermodynamics of fractals revisited with wavelets.  
490 *Physica A* 213, 232–275
- 491 Arneodo, A., Bacry, E., and Muzy, J.-F. (1998b). Random cascades on wavelet dyadic trees. *J. Math. Phys.*  
492 39, 4142–4164
- 493 Arneodo, A., Decoster, N., Kestener, P., and Roux, S. G. (2003). A wavelet-based method for multifractal  
494 image analysis: from theoretical concepts to experimental applications. *Adv. Imaging Electr. Phys.* 126,  
495 1–92

- 496 Arneodo, A., Decoster, N., and Roux, S. G. (2000). A wavelet-based method for multifractal image  
497 analysis. I. Methodology and test applications on isotropic and anisotropic random rough surfaces. *Eur.*  
498 *Phys. J.* 15, 567–600
- 499 Arneodo, A., Grasseau, G., and Holschneider, M. (1988). Wavelet transform of multifractals. *Phys. Rev.*  
500 *Lett.* 61, 2281–2284
- 501 Arneodo, A., Grasseau, G., and Kostelich, E. J. (1987). Fractal dimensions and  $f(\alpha)$  spectrum of the  
502 Hénon attractor. *Phys. Lett. A* 124, 426–432
- 503 Arneodo, A., Manneville, S., and Muzy, J.-F. (1998c). Towards log-normal statistics in high Reynolds  
504 number turbulence. *Eu. Phys. J. B* 1, 129–140
- 505 Arneodo, A., Manneville, S., Muzy, J.-F., and Roux, S. G. (1999). Revealing a lognormal cascading  
506 process in turbulent velocity statistics with wavelet analysis. *Philos. Trans. R. S. London Ser. A* 357,  
507 2415–2438
- 508 Arneodo, A., Muzy, J.-F., and Sornette, D. (1998d). “Direct” causal cascade in the stock market. *Eur. Phys.*  
509 *J. B* 2, 277–282
- 510 Arneodo, A., Vaillant, C., Audit, B., Argoul, F., d’Aubenton-Carafa, Y., and Thermes, C. (2011). Multi-  
511 scale coding of genomic information: from DNA sequence to genome structure and function. *Phys. Rep.*  
512 498, 45–188
- 513 Arora, R. (2012). Recent insights into the role of the autonomic nervous system in the creation of substrate  
514 for atrial fibrillation. *Circ. Arrhythm. Electrophysiol.* 5, 859–859
- 515 Attuel, G., Gerasimova-Chechkina, E., Argoul, F., Arneodo, A., and Yahia, H. (2017). Multifractal  
516 desynchronization of the cardiac excitable cell network during atrial fibrillation. II. Modeling. *Front.*  
517 *Physiol., to be submitted*
- 518 Attuel, P., Childers, R., Cauchemez, B., Poveda, J., Mugica, J., and Coumel, P. (1982). Failure in the rate  
519 adaptation of the atrial refractory period: its relationship to vulnerability. *Int. J. Cardiol.* 2, 179–197
- 520 Attuel, P., Pellerin, D., and Gaston, J. (1989). Latent atrial vulnerability: new means of electrophysiologic  
521 investigations in paroxysmal atrial arrhythmias. In *The Atrium in Health and Disease*, eds. P. Attuel,  
522 P. Coumel, and M. Janse (Mount Kisco Futura Publishing Co., Inc). 159–200
- 523 Attuel, P., Rancurel, G., Delgatte, B., Golcher, E., Ghazoullieres, P., Friocourt, P., et al. (1986). Importance  
524 of atrial electrophysiology in the work-up of cerebral ischemic attacks. *PACE* 9, 1121–1126
- 525 Audit, B., Bacry, E., Muzy, J.-F., and Arneodo, A. (2002). Wavelet-based estimators of scaling behavior.  
526 *IEEE Trans. Info. Theory* 48, 2938–2954
- 527 Audit, B., Baker, A., Chen, C.-L., Rappailles, A., Guilbaud, G., Julienne, H., et al. (2013). Multiscale  
528 analysis of genome-wide replication timing profiles using a wavelet-based signal-processing algorithm.  
529 *Nat. Protoc.* 8, 98–110
- 530 Bacry, E., Delour, J., and Muzy, J. F. (2001). Multifractal random walk. *Phys. Rev. E* 64, 026103
- 531 Bacry, E., Muzy, J.-F., and Arneodo, A. (1993). Singularity spectrum of fractal signals from wavelet  
532 analysis: exact results. *J. Stat. Phys.* 70, 635–674
- 533 Batchelder, K. A., Tanenbaum, A. B., Albert, S., Guimond, L., Kestener, P., Arneodo, A., et al. (2014).  
534 Wavelet-based 3D reconstruction of microcalcification clusters from two mammographic views: new  
535 evidence that fractal tumors are malignant and euclidean tumors are benign. *PloS one* 9, e107580
- 536 Bertaglia, E., Tondo, C., De Simone, A., Zoppo, F., Mantica, M., Turco, P., et al. (2010). Does catheter  
537 ablation cure atrial fibrillation? Single-procedure outcome of drug-refractory atrial fibrillation ablation: a  
538 6-year multicentre experience. *Europace* 12, 181–187
- 539 Bikou, O., Thomas, D., Trappe, K., Lugenbiel, P., Kelemen, K., Koch, M., et al. (2011). Connexin 43 gene  
540 therapy prevents persistent atrial fibrillation in a porcine model. *Cardiovasc. Res.* 92, 218–225

- 541 Bohr, T. and Tél, T. (1988). The thermodynamics of fractals. In *Directions in Chaos - Volume 2.*, ed. B.-L.  
542 Hao (Singapore: World Scientific Publishing Co). 194–237
- 543 Camm, A. J., Kirchhof, P., Lip, G. Y., Schotten, U., Savelieva, I., Ernst, S., et al. (2010). Guidelines for the  
544 management of atrial fibrillation. *Eur. Heart J.* 31, 2369–2429
- 545 Castaing, B., Gagne, Y., and Hopfinger, P. J. (1990). Velocity probability density functions of high  
546 Reynolds number turbulence. *Physica D* 46, 177–200
- 547 Castaing, B., Gagne, Y., and Marchand, M. J. (1993). Log-similarity for turbulent flows? *Physica D* 68,  
548 387–400
- 549 Chudáček, V., Andén, J., Mallat, S., Abry, P., and Doret, M. (2014). Scattering transform for intrapartum  
550 fetal heart rate variability fractal analysis: a case-control study. *IEEE Trans. Biomed. Eng.* 61, 1100–1108
- 551 Ciuciu, P., Varoquaux, G., Abry, P., Sadaghiani, S., and Kleinschmidt, A. (2012). Scale-free and multifractal  
552 time dynamics of fMRI signals during rest and task. *Front. Physiol.* 3, 186
- 553 Coumel, P. (1994). Paroxysmal atrial fibrillation: A disorder of autonomic tone? *Eur. Heart J.* 15, 9–16
- 554 Coumel, P., Attuel, P., Lavallée, J., Flammang, D., Leclercq, J., and Slama, R. (1978). The atrial arrhythmia  
555 syndrome of vagal origin. *Arch. Mal. Coeur. Vaiss.* 71, 645–656
- 556 Daubechies, I. (1992). *Ten Lectures on Wavelets*. CBMS-NSF Reg. Conf. Ser. Appl. Math., vol. 61  
557 (Philadelphia: SIAM)
- 558 Decoster, N., Roux, S. G., and Arneodo, A. (2000). A wavelet-based method for multifractal image  
559 analysis. II. Applications to synthetic multifractal rough surfaces. *Eur. Phys. J.* 15, 739–764
- 560 Delour, J., Muzy, J.-F., and Arneodo, A. (2001). Intermittency of 1D velocity spatial profiles in turbulence:  
561 a magnitude cumulant analysis. *Eur. Phys. J. B* 23, 243–248
- 562 Echt, D. S., Liebson, P. R., Mitchell, L. B., Peters, R. W., Obias-Manno, D., Barker, A. H., et al. (1991).  
563 Mortality and morbidity in patients receiving encainide, flecainide, or placebo. The Cardiac Arrhythmia  
564 Suppression Trial. *N. Engl. J. Med.* 324, 781–788
- 565 Frisch, U. (1995). *Turbulence: The Legacy of Kolmogorov* (New York: Cambridge Univ. Press)
- 566 Ganesan, A. N., Shipp, N. J., Brooks, A. G., Kuklik, P., Lau, D. H., Lim, H. S., et al. (2013). Long-term  
567 outcomes of catheter ablation of atrial fibrillation: a systematic review and meta-analysis. *J. Am. Heart*  
568 *Assoc.* 2, e004549
- 569 Gerasimova, E., Audit, B., Roux, S. G., Khalil, A., Gileva, O., Argoul, F., et al. (2014). Wavelet-based  
570 multifractal analysis of dynamic infrared thermograms to assist in early breast cancer diagnosis. *Front.*  
571 *Physiol.* 5, 176
- 572 Gerasimova-Chechkina, E., Toner, B., Marin, Z., Audit, B., Roux, S. G., Argoul, F., et al. (2016).  
573 Comparative multifractal analysis of dynamic infrared thermograms and X-ray mammograms enlightens  
574 changes in the environment of malignant tumors. *Front. Physiol.* 7, 336
- 575 Goldberger, A. L., Amaral, L. A. N., Hausdorff, J. M., Ivanov, P. C., Peng, C.-K., and Stanley, H. E. (2002).  
576 Fractal dynamics in physiology: alterations with disease and aging. *Proc. Natl. Acad. Sci. USA* 99,  
577 2466–2472
- 578 Goody, M. F., Kelly, M. W., Lessard, K. N., Khalil, A., and Henry, C. A. (2010). Nr2b-mediated NAD+  
579 production regulates cell adhesion and is required for muscle morphogenesis in vivo: Nr2b and NAD+  
580 in muscle morphogenesis. *Dev. Biol.* 344, 809–826
- 581 Grant, J., Verrill, C., Coustham, V., Arneodo, A., Palladino, F., Monier, K., et al. (2010). Perinuclear  
582 distribution of heterochromatin in developing *C. elegans* embryos. *Chrom. Res.* 18, 873–885
- 583 Grossmann, A. and Morlet, J. (1984). Decomposition of Hardy functions into square integrable wavelets  
584 of constant shape. *SIAM J. Math. Anal.* 15, 723–736

- 585 Haïssaguerre, M., Jaïs, P., Shah, D. C., Takahashi, A., Hocini, M., Quiniou, G., et al. (1998). Spontaneous  
586 initiation of atrial fibrillation by ectopic beats originating in the pulmonary veins. *N. Engl. J. Med.* 339,  
587 659–666
- 588 Holschneider, M. (1988). On the wavelet transformation of fractal objects. *J. Stat. Phys.* 50, 963–993
- 589 Igarashi, T., Finet, J. E., Takeuchi, A., Fujino, Y., Strom, M., Greener, I. D., et al. (2012). Connexin gene  
590 transfer preserves conduction velocity and prevents atrial fibrillation. *Circulation* 125, 216–225.
- 591 Ito, H. and Glass, L. (1991). Spiral breakup in a new model of discrete excitable media. *Phys. Rev. Lett.*  
592 66, 671–674
- 593 Ivanov, P. C., Amaral, L. A. N., Goldberger, A. L., Havlin, S., Rosenblum, M. G., Stanley, H. E., et al.  
594 (2001). From 1/f noise to multifractal cascades in heartbeat dynamics. *Chaos* 11, 641–652
- 595 Ivanov, P. C., Amaral, L. A. N., Goldberger, A. L., Havlin, S., Rosenblum, M. G., Struzik, Z. R., et al.  
596 (1999). Multifractality in human heartbeat dynamics. *Nature* 399, 461–465
- 597 Iwasaki, Y.-K., Nishida, K., Kato, T., and Nattel, S. (2011). Atrial fibrillation pathophysiology: implications  
598 for management. *Circulation* 124, 2264–2274
- 599 Jaffard, S. (1989). Hölder exponents at given points and wavelet coefficients. *C. R. Acad. Sci. Paris Ser. I*  
600 308, 79–81
- 601 Jaffard, S. (1997a). Multifractal formalism for functions part I: results valid for all functions. *SIAM J.*  
602 *Math. Anal.* 28, 944–970
- 603 Jaffard, S. (1997b). Multifractal formalism for functions part II: self-similar functions. *SIAM J. Math. Anal.*  
604 28, 971–998
- 605 Jaffard, S., Lashermes, B., and Abry, P. (2007). Wavelet leaders in multifractal analysis. In *Wavelet*  
606 *Analysis and Applications*, eds. T. Qian, M. I. Vai, and Y. Xu (Basel: Birkhäuser Basel, Switzerland).  
607 201–246
- 608 Janse, M. J. (1997). Why does atrial fibrillation occur? *Eur. Heart J.* 18, C12–C18
- 609 Karma, A. (1993). Spiral breakup in model equations of action potential propagation in cardiac tissue. *Phy.*  
610 *Rev. Lett.* 71, 1103–1106
- 611 Kestener, P. and Arneodo, A. (2003). Three-dimensional wavelet-based multifractal method: The need for  
612 revisiting the multifractal description of turbulence dissipation data. *Phys. Rev. Lett.* 91, 194501
- 613 Kestener, P. and Arneodo, A. (2004). Generalizing the wavelet-based multifractal formalism to random  
614 vector fields: Application to three-dimensional turbulence velocity and vorticity data. *Phys. Rev. Lett.* 93,  
615 044501
- 616 Kestener, P., Conlon, P. A., Khalil, A., Fennell, L., McAteer, R., Gallagher, P. T., et al. (2010).  
617 Characterizing complexity in solar magnetogram data using a wavelet-based segmentation method.  
618 *Astrophys. J.* 717, 995
- 619 Kestener, P., Lina, J.-M., Saint-Jean, P., and Arneodo, A. (2001). Wavelet-based multifractal formalism to  
620 assist in diagnosis in digitized mammograms. *Image Anal. Stereol.* 20, 169–174
- 621 Khalil, A., Aponte, C., Zhang, R., Davisson, T., Dickey, I., Engelman, D., et al. (2009). Image analysis of  
622 soft-tissue in-growth and attachment into highly porous alumina ceramic foam metals. *Med. Eng. Phys.*  
623 31, 775–783
- 624 Khalil, A., Grant, J. L., Caddle, L. B., Atzema, E., Mills, K. D., and Arneodo, A. (2007). Chromosome  
625 territories have a highly nonspherical morphology and nonrandom positioning. *Chrom. Res.* 15, 899–916
- 626 Khalil, A., Joncas, G., Nekka, F., Kestener, P., and Arnéodo, A. (2006). Morphological analysis of HI  
627 features. II. Wavelet-based multifractal formalism. *Astrophys. J. Suppl. Ser.* 165, 512–550
- 628 Kolmogorov, A. N. (1962). A refinement of previous hypotheses concerning the local structure of turbulence  
629 in a viscous incompressible fluid at high Reynolds number. *J. Fluid Mech.* 13, 82–85

- 630 Konings, K. T., Kirchhof, C. J., Smeets, J. R., Wellens, H. J., Penn, O. C., and Allessie, M. A. (1994).  
631 High-density mapping of electrically induced atrial fibrillation in humans. *Circulation* 89, 1665–1680
- 632 Konings, K. T., Smeets, J. L., Penn, O. C., Wellens, H. J., and Allessie, M. A. (1997). Configuration of  
633 unipolar atrial electrograms during electrically induced atrial fibrillation in humans. *Circulation* 95,  
634 1231–1241
- 635 Lip, G. Y. and Lane, D. A. (2015). Stroke prevention in atrial fibrillation: a systematic review. *JAMA* 313,  
636 1950–1962
- 637 Mallat, S. (1998). *A Wavelet Tour of Signal Processing* (New York: Academic Press)
- 638 Mallat, S. and Hwang, W. L. (1992). Singularity detection and processing with wavelets. *IEEE Trans. Inf.*  
639 *Theory* 38, 617–643
- 640 Mandelbrot, B. B. (1974). Intermittent turbulence in self similar cascades; divergence of high moments  
641 and dimension of the carrier. *J. Fluid Mech.* 62, 331–358
- 642 Mandelbrot, B. (1982). *The Fractal Geometry of Nature* (San Francisco: Freeman)
- 643 Mandelbrot, B. (1998). *Multifractal noise and 1/f noise : Wild self-affinity in physics* (New York: Springer)
- 644 Marin, Z., Batchelder, K. A., Toner, B. C., Guimond, L., Gerasimova-Chechkina, E., Harrow, A. R., et al.  
645 (2017). Mammographic evidence of microenvironment changes in tumorous breasts. *Med. Phys.* 44,  
646 1324–1336
- 647 Martinez-Torres, C., Berguiga, L., Streppa, L., Boyer-Provera, E., Schaeffer, L., Elezgaray, J., et al. (2014).  
648 Diffraction phase microscopy: retrieving phase contours on living cells with a wavelet-based space-scale  
649 analysis. *J. Biomed. Opt.* 19, 036007
- 650 Martinez-Torres, C., Laperrousaz, B., Berguiga, L., Boyer-Provera, E., Elezgaray, J., Nicolini, F. E.,  
651 et al. (2015). Deciphering the internal complexity of living cells with quantitative phase microscopy: a  
652 multiscale approach. *J. Biomed. Opt.* 20, 096005
- 653 McAteer, R. T. J., Kestener, P., Arneodo, A., and Khalil, A. (2010). Automated detection of coronal loops  
654 using a wavelet transform modulus maxima method. *Solar Phys.* 262, 387–397
- 655 Meneveau, C. and Sreenivasan, K. (1991). The multifractal nature of turbulent energy dissipation. *J. Fluid*  
656 *Mech.* 224, 429–484
- 657 Meyer, Y. (1992). *Wavelets and Operators* (Cambridge: Cambridge Univ. Press)
- 658 Middlekauff, H. R., Stevenson, W. G., and Stevenson, L. W. (1991). Prognostic significance of atrial  
659 fibrillation in advanced heart failure. *Circulation* 84, 40–48
- 660 Misier, A. R., Opthof, T., van Hemel, N. M., Defauw, J. J., de Bakker, J. M., Janse, M. J., et al. (1992).  
661 Increased dispersion of 'refractoriness' in patients with idiopathic paroxysmal atrial fibrillation. *J. Am.*  
662 *Coll. Cardiol.* 19, 1531–1535
- 663 Moe, G. K. and Abildskov, J. A. (1959). Atrial fibrillation as a self-sustaining arrhythmia independent of  
664 focal discharge. *Am. Heart J.* 58, 59–70
- 665 Moe, G. K., Rheinboldt, W. C., and Abildskov, J. A. (1964). A computer model of atrial fibrillation. *Am.*  
666 *Heart J.* 67, 200–220
- 667 Muzy, J.-F., Bacry, E., and Arneodo, A. (1991). Wavelets and multifractal formalism for singular signals:  
668 Application to turbulence data. *Phys. Rev. Lett.* 67, 3515–3518
- 669 Muzy, J.-F., Bacry, E., and Arneodo, A. (1993). Multifractal formalism for fractal signals: The structure-  
670 function approach versus the wavelet-transform modulus-maxima methods. *Phys. Rev. E* 47, 875–884
- 671 Muzy, J.-F., Bacry, E., and Arneodo, A. (1994). The multifractal formalism revisited with wavelets. *Int. J.*  
672 *Bifurc. Chaos* 4, 245–302
- 673 Muzy, J. F., Delour, J., and Bacry, E. (2000). Modelling fluctuations of financial time series: from cascade  
674 process to stochastic volatility model. *Eur. Phys. J. B* 17, 537–548

- 675 Muzy, J.-F., Sornette, D., Delour, J., and Arneodo, A. (2001). Multifractal returns and hierarchical portfolio  
676 theory. *Quant. Finance* 1, 131–148
- 677 Nademanee, K., McKenzie, J., Kosar, E., Schwab, M., Sunsaneewitayakul, B., Vasavakul, T., et al. (2004).  
678 A new approach for catheter ablation of atrial fibrillation: Mapping of the electrophysiologic substrate. *J.*  
679 *Am. Coll. Cardiol.* 43, 2044–2053
- 680 Nattel, S., Burstein, B., and Dobrev, D. (2008). Atrial remodeling and atrial fibrillation mechanisms and  
681 implications. *Circ. Arrhythm. Electrophysiol.* 2, 62–73
- 682 Nattel, S. and Harada, M. (2014). Atrial remodeling and atrial fibrillation: recent advances and translational  
683 perspectives. *J. Am. Coll. Cardiol.* 63, 2335–2345
- 684 Nicolay, S., Brodie of Brodie, E. B., Touchon, M., Audit, B., d'Aubenton Carafa, Y., Thermes, C., et al.  
685 (2007). Bifractality of human DNA strand-asymmetry profiles results from transcription. *Phys. Rev. E*  
686 75, 032902
- 687 Oboukhov, A. M. (1962). Some specific features of atmospheric turbulence. *J. Fluid Mech.* 13, 77–81
- 688 Rensma, P. L., Allessie, M. A., Lammers, W. J., Bonke, F. I., and Schalij, M. J. (1988). Length of excitation  
689 wave and susceptibility to reentrant atrial arrhythmias in normal conscious dogs. *Circ. Res.* 62, 395–410
- 690 Richard, C. D., Tanenbaum, A., Audit, B., Arneodo, A., Khalil, A., and Frankel, W. N. (2015). Swdreader:  
691 A wavelet-based algorithm using spectral phase to characterize spike-wave morphological variation in  
692 genetic models of absence epilepsy. *J. Neurosci. Methods* 242, 127–140
- 693 Roland, T., Khalil, A., Tanenbaum, A., Berguiga, L., Delichère, P., Bonneviot, L., et al. (2009). Revisiting  
694 the physical processes of vapodeposited thin gold films on chemically modified glass by atomic force  
695 and surface plasmon microscopies. *Surf. Sci.* 603, 3307–3320
- 696 Roux, S. G., Arneodo, A., and Decoster, N. (2000). A wavelet-based method for multifractal image analysis.  
697 III. Applications to high-resolution satellite images of cloud structure. *Eur. Phys. J.* 15, 765–786
- 698 Roux, S. G., Venugopal, V., Fienberg, K., Arneodo, A., and Foufoula-Georgiou, E. (2009). Evidence for  
699 inherent nonlinearity in temporal rainfall. *Adv. Water Resour.* 32, 41–48
- 700 Roy, D., Talajic, M., Nattel, S., Wyse, D. G., Dorian, P., Lee, K. L., et al. (2008). Rhythm control versus  
701 rate control for atrial fibrillation and heart failure. *N. Engl. J. Med.* 358, 2667–2677
- 702 Severs, N. J., Bruce, A. F., Dupont, E., and Rothery, S. (2008). Remodelling of gap junctions and connexin  
703 expression in diseased myocardium. *Cardiovasc. Res.* 80, 9–19
- 704 Smeets, J. L., Allessie, M. A., Lammers, W. J., Bonke, F. I., and Hollen, J. (1986). The wavelength of the  
705 cardiac impulse and reentrant arrhythmias in isolated rabbit atrium. The role of heart rate, autonomic  
706 transmitters, temperature, and potassium. *Circ. Res.* 58, 96–108
- 707 Snow, C. J., Goody, M., Kelly, M. W., Oster, E. C., Jones, R., Khalil, A., et al. (2008). Time-lapse analysis  
708 and mathematical characterization elucidate novel mechanisms underlying muscle morphogenesis. *PLoS*  
709 *Genet.* 4, e1000219
- 710 Stevenson, W. G. and Stevenson, L. W. (1999). Atrial fibrillation in heart failure. *N. Eng. J. Med.* 341,  
711 910–911
- 712 Takigawa, M., Takahashi, A., Kuwahara, T., Okubo, K., Takahashi, Y., Watari, Y., et al. (2014). Long-  
713 term follow-up after catheter ablation of paroxysmal atrial fibrillation: the incidence of recurrence and  
714 progression of atrial fibrillation. *Circ. Arrhythm. Electrophysiol.* 7, 267–273
- 715 Tan, A. Y., Chen, P.-S., Chen, L. S., and Fishbein, M. C. (2007). Autonomic nerves in pulmonary veins.  
716 *Heart Rythm* 4, S57–S60
- 717 The CAST II investigators (1992). The Cardiac Arrhythmia Suppression Trial. *N. Engl. J. Med.* 327,  
718 227–233



- 719 Turiel, A., Yahia, H., and Pérez-Vicente, C. J. (2008). Microcanonical multifractal formalism – a  
720 geometrical approach to multifractal systems: Part I. Singularity analysis. *J. Phys. A: Math. Theor.* 41,  
721 015501
- 722 Ulphani, J. S., Arora, R., Cain, J. H., Villuendas, R., Shen, S., Gordon, D., et al. (2007). The ligament of  
723 Marshall as a parasympathetic conduit. *Am. J. Physiol. Heart Circ. Physiol.* 293, H1629–H1635
- 724 van Marion, D. M., Lanters, E. A., Wiersma, M., Allessie, M. A., Brundel, B. B., and de Groot, N. M.  
725 (2015). Diagnosis and therapy of atrial fibrillation: the past, the present and the future. *J. Atr. Fibrillation*  
726 8, 1216
- 727 Venugopal, V., Roux, S. G., Foufoula-Georgiou, E., and Arneodo, A. (2006). Revisiting multifractality of  
728 high-resolution temporal rainfall using a wavelet-based formalism. *Water Resour. Res.* 42, W06D14
- 729 Verma, A., Jiang, C.-Y., Betts, T. R., Chen, J., Deisenhofer, I., Mantovan, R., et al. (2015). Approaches to  
730 catheter ablation for persistent atrial fibrillation. *N. Engl. J. Med.* 372, 1812–1822
- 731 Vicsek, T. (1989). *Fractal Growth Phenomena* (Singapore: World Scientific)
- 732 Wang, T. J., Larson, M. G., Levy, D., Vasan, R. S., Leip, E. P., Wolf, P. A., et al. (2003). Temporal relations  
733 of atrial fibrillation and congestive heart failure and their joint influence on mortality. *Circulation* 107,  
734 2920–2925
- 735 Wendt, H., Abry, P., and Jaffard, S. (2007). Bootstrap for empirical multifractal analysis. *IEEE Signal*  
736 *Process. Mag.* 24, 38–48
- 737 West, B. J. and Shlesinger, M. F. (1988). The noise in natural phenomena. *American Scientist* 78, 40–45
- 738 Wijffels, M. C., Kirchhof, C. J., Dorland, R., and Allessie, M. A. (1995). Atrial fibrillation begets atrial  
739 fibrillation. A study in awake chronically instrumented goats. *Circulation* 92, 1954–1968
- 740 Wolf, P. A., Abbott, R. D., and Kannel, W. B. (1991). Atrial fibrillation as an independent risk factor for  
741 stroke: the Framingham Study. *Stroke* 22, 983–988
- 742 Wolf, P. A., Dawber, T. R., Thomas, H. E., and Kannel, W. B. (1978). Epidemiologic assessment of chronic  
743 atrial fibrillation and risk of stroke: the Framingham Study. *Neurology* 28, 973–973
- 744 Wynn, G. J., El-Kadri, M., Haq, I., Das, M., Modi, S., Snowdon, R., et al. (2016). Long-term outcomes  
745 after ablation of persistent atrial fibrillation: an observational study over 6 years. *Open Heart* 3, e000394
- 746 Yue, L., Feng, J., Gaspo, R., Li, G.-R., Wang, Z., and Nattel, S. (1997). Ionic remodeling underlying action  
747 potential changes in a canine model of atrial fibrillation. *Circ. Res.* 81, 512–525
- 748 Zipes, D. P., Jalife, J., and Stevenson, W. G. (2017). *Cardiac Electrophysiology: from cell to bedside*  
749 (Philadelphia: Elsevier Saunders)

## TABLES

**Table 1.** Results of the WTMM multifractal analysis of the local impulse energy time-series recorded along the CS vein at electrodes Pt1, Pt2, Pt3 and Pt5.

Point1			
	$g^{(1)}$	$g^{(2)}$	$g^{(3)}$
$c_0$	$0.961\pm 0.001$	$0.995\pm 0.001$	$1.009\pm 0.002$
$c_1$	$-0.351\pm 0.003$	$-0.298\pm 0.005$	$-0.281\pm 0.007$
$c_1^*$	$-0.353\pm 0.017$	$-0.297\pm 0.011$	$-0.274\pm 0.011$
$c_2$	$0.048\pm 0.006$	$0.063\pm 0.011$	$0.064\pm 0.014$
$c_2^*$	$0.050\pm 0.032$	$0.082\pm 0.018$	$0.096\pm 0.020$

Point2			
	$g^{(1)}$	$g^{(2)}$	$g^{(3)}$
$c_0$	$1.011\pm 0.002$	$0.998\pm 0.001$	$1.011\pm 0.001$
$c_1$	$-0.333\pm 0.007$	$-0.348\pm 0.003$	$-0.337\pm 0.005$
$c_1^*$	$-0.307\pm 0.012$	$-0.335\pm 0.011$	$-0.331\pm 0.011$
$c_2$	$0.055\pm 0.013$	$0.049\pm 0.007$	$0.053\pm 0.010$
$c_2^*$	$0.076\pm 0.030$	$0.031\pm 0.027$	$0.047\pm 0.028$

Point3			
	$g^{(1)}$	$g^{(2)}$	$g^{(3)}$
$c_0$	$1.023\pm 0.003$	$1.005\pm 0.002$	$1.021\pm 0.003$
$c_1$	$-0.472\pm 0.014$	$-0.496\pm 0.008$	$-0.481\pm 0.011$
$c_1^*$	$-0.445\pm 0.011$	$-0.480\pm 0.008$	$-0.464\pm 0.007$
$c_2$	$0.082\pm 0.028$	$0.091\pm 0.015$	$0.098\pm 0.022$
$c_2^*$	$0.164\pm 0.031$	$0.103\pm 0.023$	$0.164\pm 0.020$

Point5			
	$g^{(1)}$	$g^{(2)}$	$g^{(3)}$
$c_0$	$1.044\pm 0.003$	$1.017\pm 0.003$	$1.029\pm 0.002$
$c_1$	$-0.320\pm 0.014$	$-0.365\pm 0.011$	$-0.383\pm 0.009$
$c_1^*$	$-0.256\pm 0.015$	$-0.335\pm 0.018$	$-0.365\pm 0.025$
$c_2$	$0.176\pm 0.028$	$0.167\pm 0.022$	$0.152\pm 0.018$
$c_2^*$	$0.175\pm 0.043$	$0.106\pm 0.029$	$0.114\pm 0.031$

750  $c_0, c_1, c_2$  are the coefficients of the polynomial expansion of  $\tau(q)$  (Eq. (10)) obtained with the WTMM  
 751 method of moments when using the analyzing wavelets  $g^{(1)}, g^{(2)}$  and  $g^{(3)}$  respectively (Figure S1).  $c_1^*$  and  
 752  $c_2^*$  are the corresponding coefficients obtained with the magnitude cumulant method.

## FIGURES

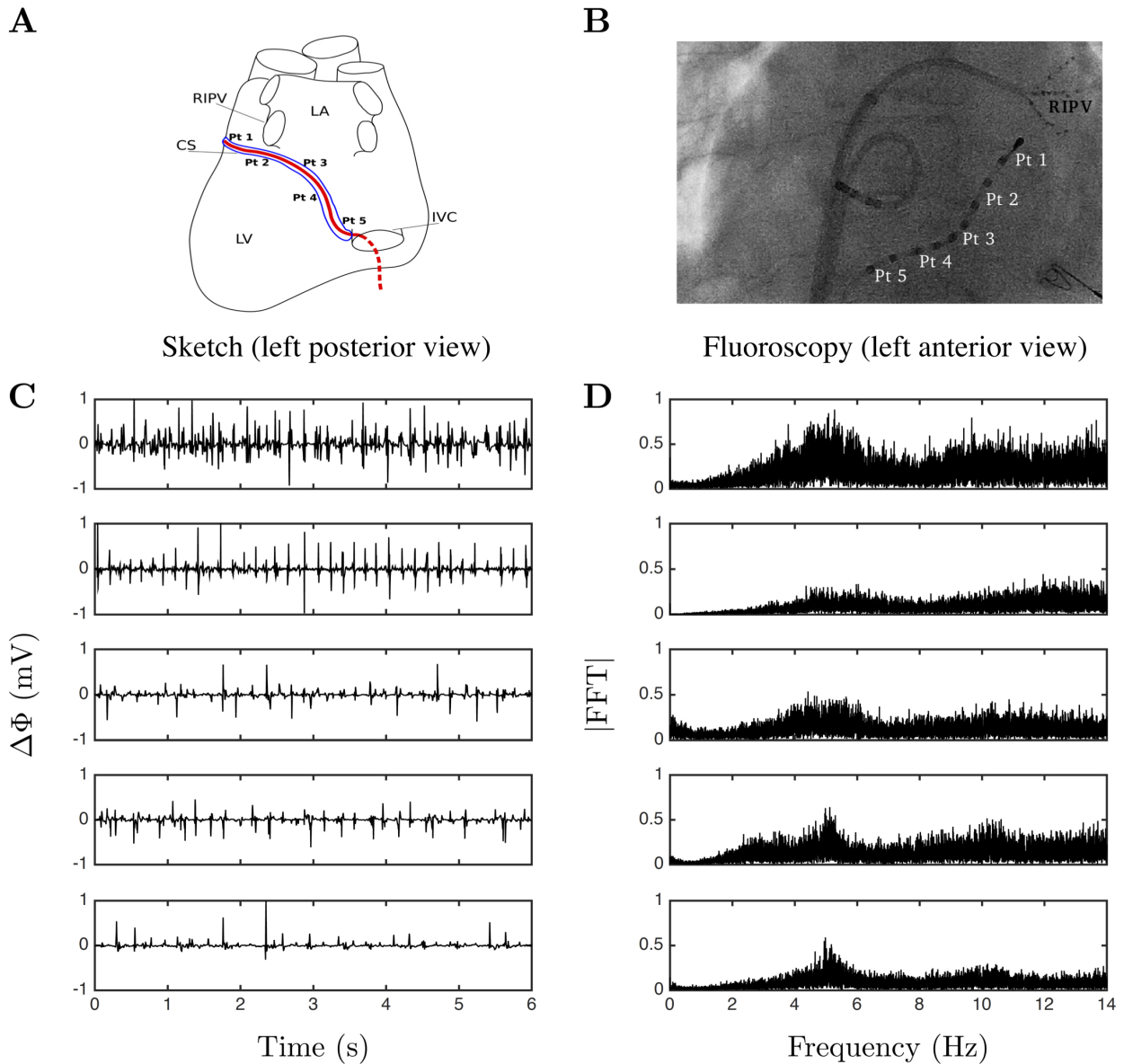


**Figure 1.** Electric potential recording. (A) Sketch of the positioning of the pairs of electrodes (Pt1 to Pt5) along the catheter in the coronary sinus (CS); left posterior view of the heart left ventricle (LV), right inferior pulmonary vein (RIPV), left atrium (LA), and inferior vena cava (IVC). (B) A radiography of the atria showing the pairs of electrodes in the CS. (C) 6 s portions of  $\Delta\phi(t)$  recorded at the points Pt1, Pt2, Pt3, Pt4 and Pt5, from top to bottom. (D) Corresponding Fourier power spectra computed over the whole 422 s time series.

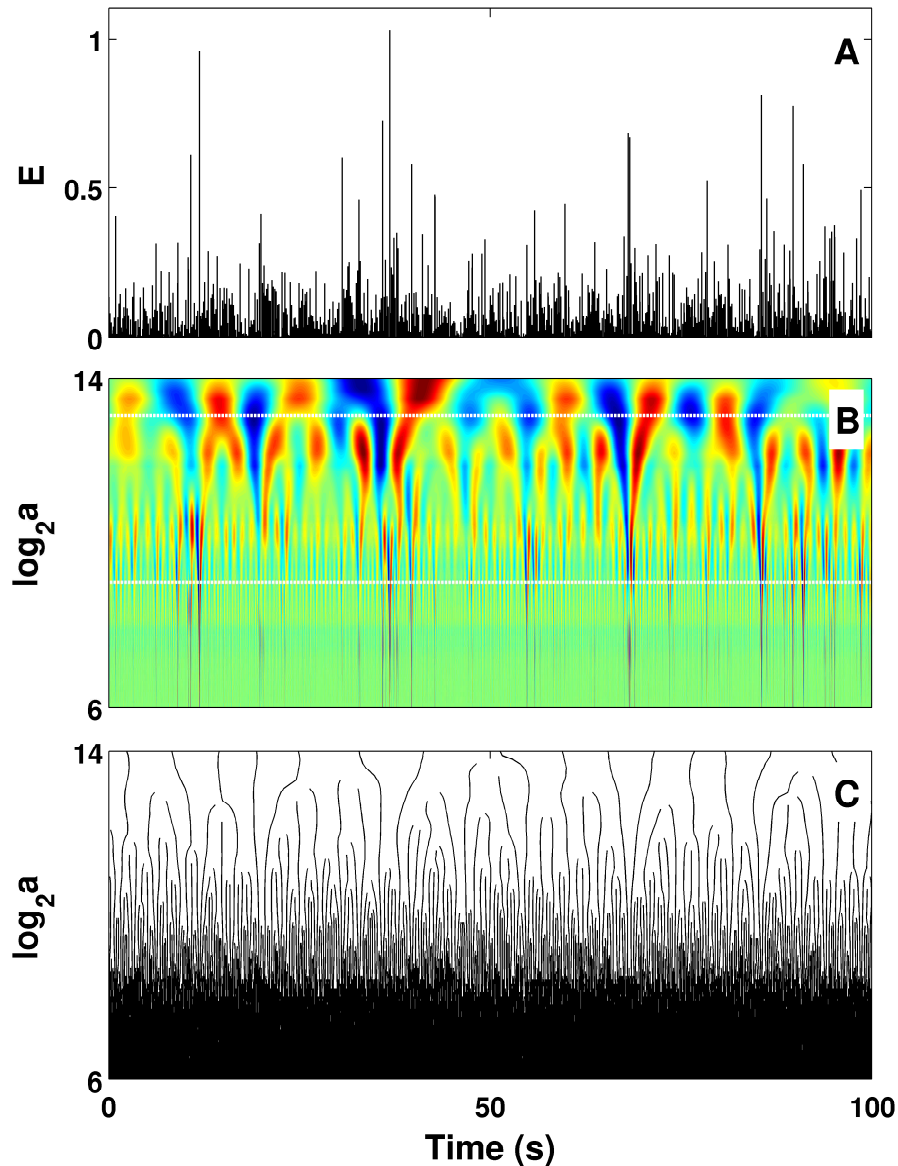


**Figure 2.** Wavelet transform of local impulse energy time-series. (A) A 100 s portion of  $E(t)$  (Eq. (19)) recorded at the electrode Pt2. (B) Time-scale WT representation of  $E(t)$  with the analyzing wavelet  $g^{(3)}$  (Figure S1). The modulus of the WT is coded, independently at each scale  $a$ , using 256 colors from black ( $|T_{g^{(3)}}(t, a)| = 0$ ) to red ( $\max_t |T_{g^{(3)}}(t, a)|$ ). (C) WT skeleton defined by the maxima lines. The scale  $a = \Delta t / \Delta t_0$ , where  $\Delta t_0 = 10^{-4}$  s. In (B) the white horizontal dotted lines delimit the range of time scales ( $2^9 \leq a \leq 2^{13}$ ) used to perform linear regression fit estimates of the  $\tau(q)$  and  $D(h)$  multifractal spectra.

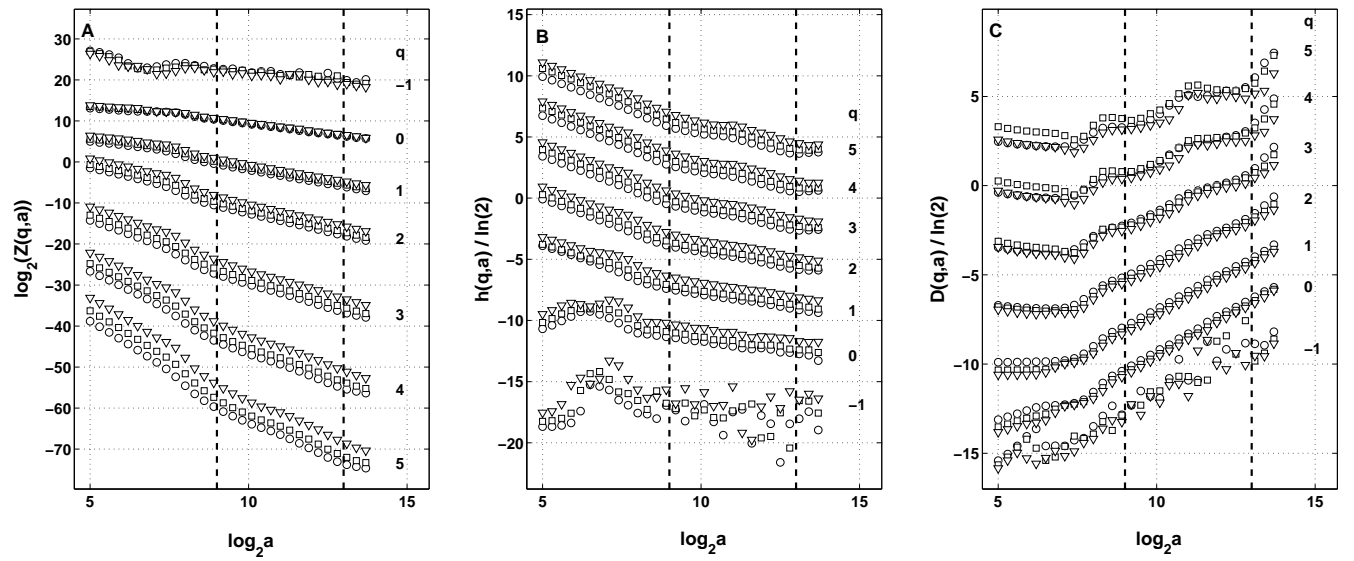


**Figure 3.** Multifractal analysis of local impulse energy time-series recorded at the electrode Pt2 with the WTMM method. (A)  $\log_2 Z(q, a)$  vs  $\log_2 a$  (Eq. (3)). (B)  $h(q, a) / \ln 2$  vs  $\log_2 a$  (Eq. (5)). (C)  $D(q, a) / \ln 2$  vs  $\log_2 a$  (Eq. (6)). The computation was performed for different values from  $q = -1$  to 5 with the analyzing wavelet  $g^{(1)}$  ( $\nabla$ ),  $g^{(2)}$  ( $\square$ ) and  $g^{(3)}$  ( $\circ$ ) (Figure S1). The vertical dashed lines delimit the range of scale ( $2^9 \leq a \leq 2^{13}$ ) used for the linear regression estimate of  $\tau(q)$ ,  $h(q)$  and  $D(q)$  in Figure 4.

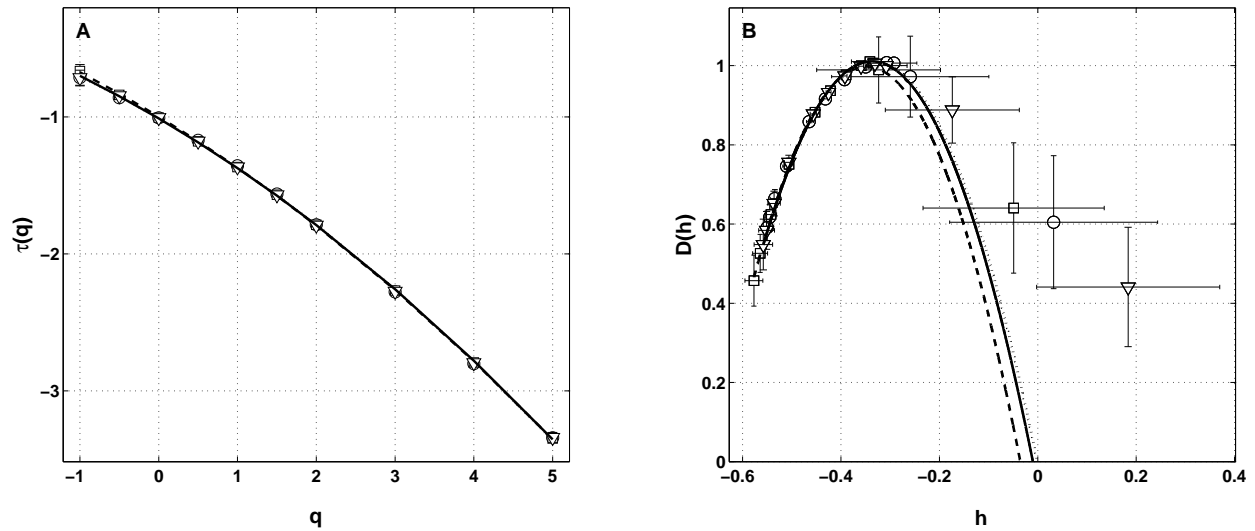


**Figure 4.** Multifractal spectra of local impulse energy time-series (Pt2) obtained with the WTMM method of moments. (A)  $\tau(q)$  vs  $q$  estimated by linear regression fit of  $\log_2 Z(q, a)$  vs  $\log_2 a$  (Figure 3A). (B)  $D(h)$  vs  $h$  obtained from linear regression fits of  $h(q, a)$  (Figure 3B) and  $D(q, a)$  (Figure 3C) vs  $\log_2 a$ . The symbols correspond to the analyzing wavelets  $g^{(1)}$  ( $\nabla$ ),  $g^{(2)}$  ( $\square$ ) and  $g^{(3)}$  ( $\circ$ ) (Figure S1). The curves correspond to quadratic spectra (Eqs (10) and (12)) with parameters  $[c_0, c_1, c_2] = [1.01, -0.33, 0.055]$  ( $\cdots$ ,  $g^{(1)}$ ),  $[1.00, -0.35, 0.049]$  ( $- - -$ ,  $g^{(2)}$ ),  $[1.01, -0.34, 0.053]$  ( $—$ ,  $g^{(3)}$ ) (see Table 1).



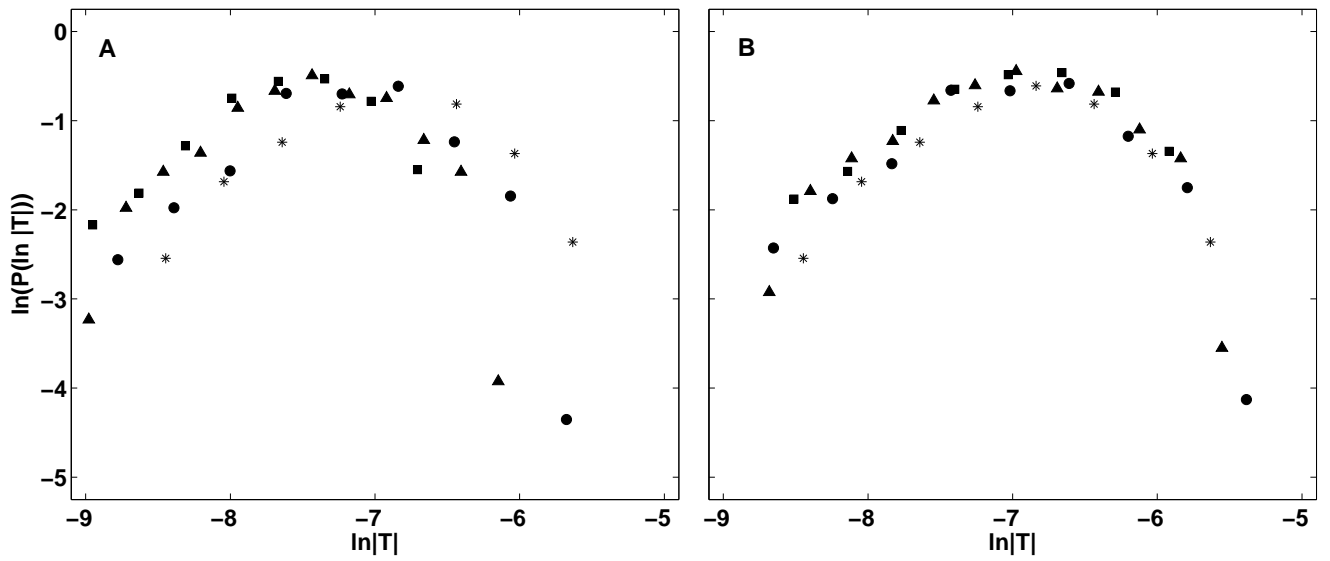


**Figure 5.** Demonstration of the WTMM pdf rescaling via the propagative equation across scales (Eq. (13)). (A) Original pdfs of the logs of WTMM coefficients (magnitude coefficients) of the local impulse energy time series recorded at the electrode Pt2, computed with the analyzing wavelet  $g^{(3)}$ , at scales  $a (= \Delta t / \Delta t_0$ , where  $\Delta t_0 = 10^{-4}$  s)  $= 2^9$  (\*),  $2^{10}$  (●),  $2^{11}$  (▲) and  $2^{12}$  (■). (B) Rescaled pdfs using the multifractal quadratic estimate of the  $\tau(q)$  spectrum (Eq. (10)) with parameters  $[c_0, c_1, c_2] = [1.01, -0.34, 0.053]$  (see Table 1).

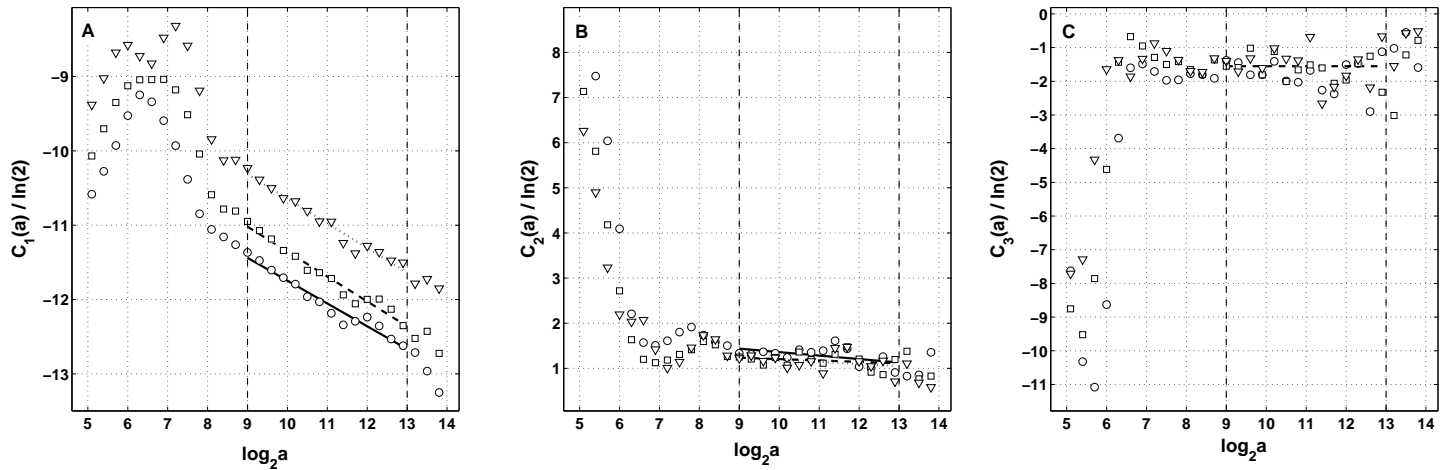


**Figure 6.** Magnitude cumulant analysis of local impulse energy time-series (Pt2). (A)  $C_1(a)/\ln 2$  vs  $\log_2 a$ . (B)  $C_2(a)/\ln 2$  vs  $\log_2 a$ . (C)  $C_3(a)/\ln 2$  vs  $\log_2 a$ . The computation of the  $C_n(a)$  (Eq. (9)) was performed with the analyzing wavelets  $g^{(1)}$  ( $\nabla$ ),  $g^{(2)}$  ( $\square$ ) and  $g^{(3)}$  ( $\circ$ ) (Figure S1). The vertical dashed lines delimit the range of scales ( $2^9 \leq a \leq 2^{13}$ ) used for the linear regression estimate of coefficients  $c_1^*$ ,  $c_2^*$  and  $c_3^*$  of  $\tau(q)$  (Eq. (10)) reported in Table 1.

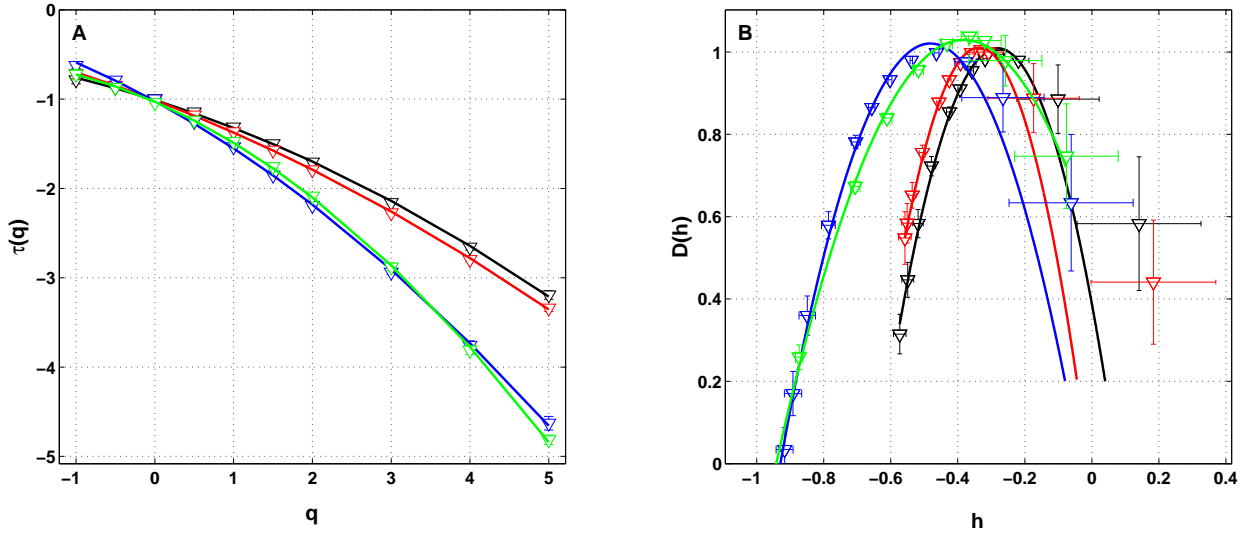


**Figure 7.** Multifractal spectra of local impulse energy time-series recorded along the CS vein. (A)  $\tau(q)$  vs  $q$  estimated by linear regression fit of  $\log_2 Z(q, a)$  vs  $\log_2 a$ . (B)  $D(h)$  vs  $h$  obtained from linear regression fits of  $h(q, a)$  and  $D(q, a)$  vs  $\ln_2 a$ . The analyzing wavelets is  $g^{(3)}$ . The colored symbols correspond to the electrodes Pt1 (black), Pt2 (red), Pt3 (blue) and Pt5 (green). The curves correspond to quadratic spectra (Eqs (10) and (12)) with parameters  $[c_0, c_1, c_2] = [1.01, -0.28, 0.064]$  (black, Pt1),  $[1.01, -0.34, 0.053]$  (red, Pt2),  $[1.02, -0.48, 0.098]$  (blue, Pt3), and  $[1.03, -0.38, 0.152]$  (green, Pt5) (see Table 1).

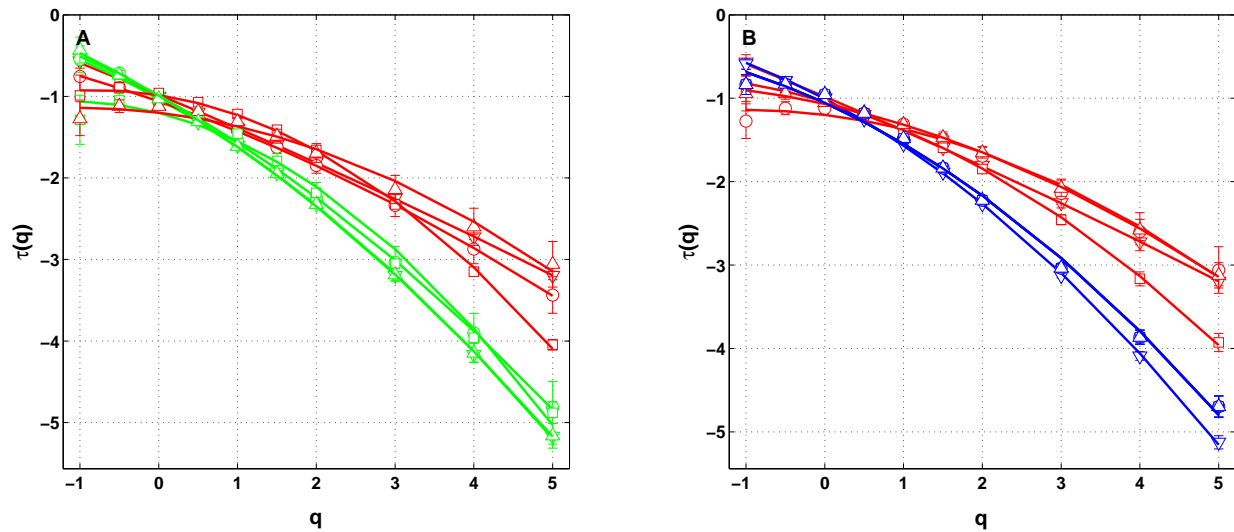


**Figure 8.**  $\tau(q)$  spectra of local impulse energy time-series recorded along the CS vein at the electrodes Pt2 (red), Pt3 (blue) and Pt5 (green). The curves represent quadratic polynomial fit of the data (Eq. (10)). (A) The symbols correspond to the reference Patient 1 (chronic AF,  $\nabla$ ) and to Patients 2 (chronic AF,  $\circ$ ), 3 (paroxysmal AF,  $\square$ ) and 4 (persistent AF,  $\triangle$ ). (B) The symbols correspond to the reference Patient 1 ( $\nabla$ ) and to three different time-series for Patient 4 ( $\circ$ ,  $\square$ ,  $\triangle$ ) recorded at different periods of time preceding ablation procedure.

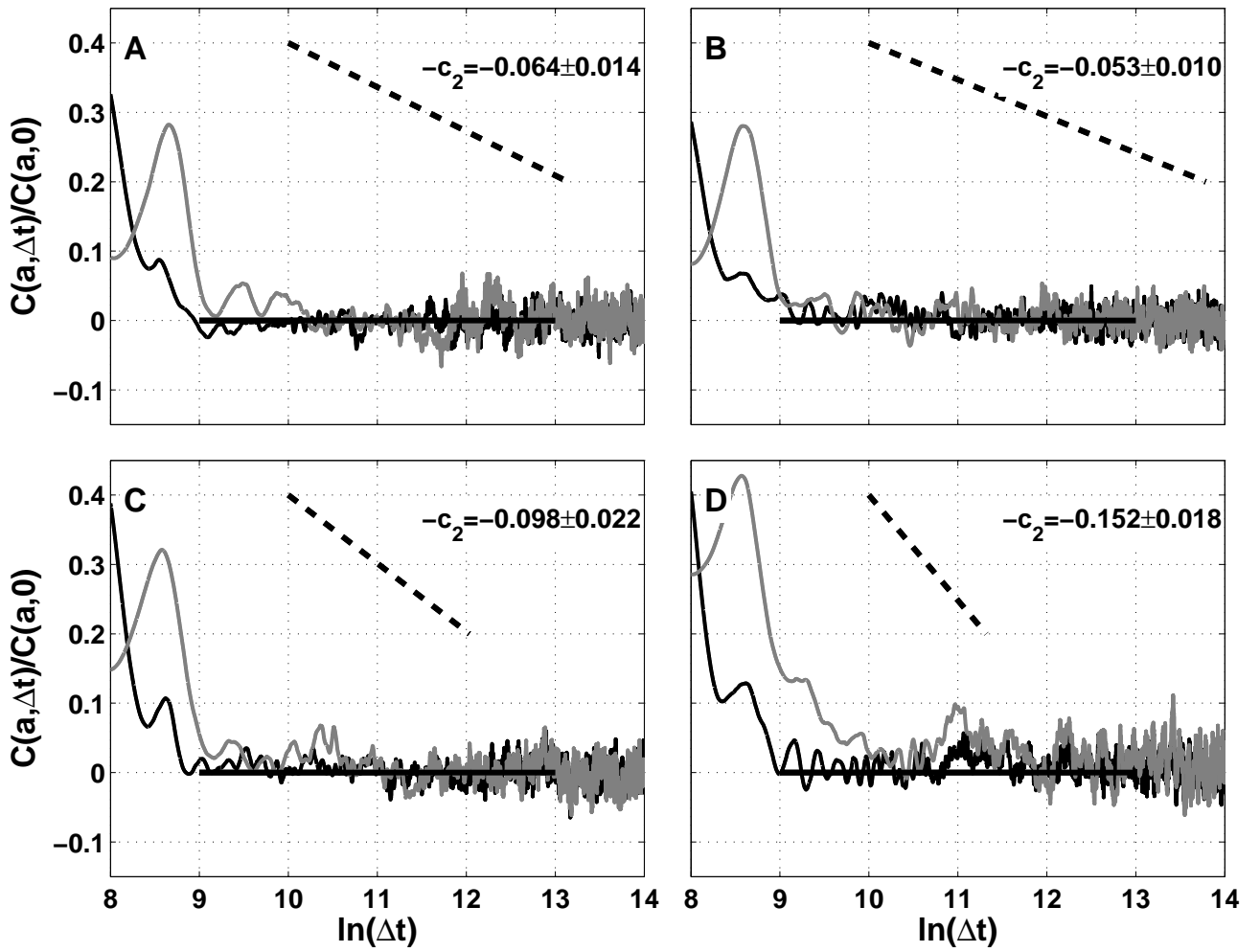


**Figure 9.** Two-point magnitude analysis of local impulse energy time-series recorded along the CS vein. Two-point correlation function  $C(a, \Delta t)/C(a, 0)$  vs  $\ln(\Delta t)$  (Eq. (15)) for local impulse energy  $E(t)$  computed with the analyzing wavelet  $g^{(3)}$ . The two curves correspond to scales  $a = 2^9$  (black) and  $2^{10}$  (grey) within the scaling range. (A) Pt1, (B) Pt2, (C) Pt3, and (D) Pt5.